Title
Mid-infrared Quantum Cascade Lasers Modeling, Fabrication and Characterization

Author
Xu, Luyao

Publication Date
2013

Peer reviewed|Thesis/dissertation

University of California
Los Angeles

Mid-infrared Quantum Cascade Lasers Modeling, Fabrication and Characterization

A thesis submitted in partial satisfaction
of the requirements for the degree
Master of Science in Electrical Engineering

by

Luyao Xu

2013

Abstract of the Thesis

Mid-infrared Quantum Cascade Lasers Modeling, Fabrication and Characterization

by

Luyao Xu

Master of Science in Electrical Engineering

University of California, Los Angeles, 2013

Professor Benjamin Williams, Chair

In the past 20 years, mid-infrared Quantum Cascade Lasers (mid-IR QCLs) have been experiencing rapid development and have become practical mid-IR sources for a variety of applications. There is particular technological interest in high efficiency lasers designed for the midwave infrared (MWIR) atmospheric window (3-5 μm) and longwave infrared (LWIR) atmospheric window (8-13 μm). This work presents a systematic study over mid-IR QCLs, including theoractical modeling, device fabrication and characterization. An effective bandstructure calculation method is implemented in this work for active region modeling. A standard process for fabricating mid-IR QCLs has been developed, based on which both LWIR ($\sim$9 μm) and MWIR ($\sim$4 μm) QCLs have been successfully demonstrated. Comprehensive testing results are analyzed and discussed, yielding valuable information about the current device design.

The thesis of Luyao Xu is approved.

Oscar Stafsudd

Chandrashekar Joshi

Benjamin Williams, Committee Chair

University of California, Los Angeles

2013

Table of Contents

1 Introduction **1**

1.1 Mid-infrared applications and sources 2

1.2 Overview of mid-infrared quantum cascade lasers 3

1.2.1 Bandstructure and optical gain 4

1.2.2 Waveguide and loss 9

1.2.3 Performance parameters 11

1.3 Thesis overview 13

2 QCL bandstructure modeling and solver **14**

2.1 Introduction 14

2.2 Intersubband laser theory 14

2.2.1 Electronic states in quantum wells 15

2.2.2 Intersubband radiative transitions 18

2.2.3 Inter- and intra-subband nonradiative transitions 21

2.3 Bandstructure solver 24

2.3.1 Shooting method 24

2.3.2 Solution to a single square quantum well 26

2.3.3 Solution to QCL bandstructures and transition rates calculation 28

3 QCL ridge waveguide fabrication and modeling **33**

3.1 Introduction 33

3.2 Overview of ridge waveguide structures 33

3.3 QCL ridge waveguide fabrication 34
3.4 Fabrication results 36
3.5 Optical mode in ridge waveguides 36

4 Device testing, characterization and discussion 40
4.1 Introduction 40
4.2 Device mounting 40
4.3 LIV measurement and temperature performance 41
4.4 Loss and gain measurement 44
4.5 Spectra measurement 49
4.6 Beam pattern measurement 51

5 Conclusions 54

A Processing recipes 56
A.1 AZ5214E Photolithography 56
A.2 NLOF 2020 Photolithography 56
A.3 PECVD growth recipe 57
A.4 Dry etching recipe 57

References 58

List of Figures

1.1 Simple correlations of various group molecular vibrations. Figure from [8]. 3

1.2 Schematic timeline of major developments in QCLs. Figure from [17]. 5

1.3 (a) Schematic of a deep-etched, ridge waveguide QCL. The brown arrow indicates the laser emission. (b) A Transimission Electron Microscopy (TEM) image of the active core of a QCL. The dark layers are the $In_{0.52}Al_{0.48}As$ barriers, and the bright layers are the $In_{0.53}Ga_{0.47}As$ wells. (c) Conduction band diagram of one active region sandwiched by two injectors and the moduli squared of relevant wavefunctions. Figure from [17] 6

1.4 A three-level laser system model for QCLs. 6

1.5 Total WPE of selected lasers from the literature at various heat sink temperatures for pulsed and CW operation. Figure from [14]. 13

2.1 Comparison between an intersubband transition (a) and an interband transition in a quantum well. Figure from [23]. 15

2.2 (a) Schematic illustration of intersubband LO-phonon scattering process in k-space. (b) In-plane diagram illustrating the relationship between initial and final electron wavevectors k_i and k_f and in-plane phonon wavevector. Figure from [18]. 22

2.3 The eigen-wavefunctions of localized eigen-states solved by ST solver for (a) a 20 Å-wide well and (b) a 200 Å-wide well. 28

2.4 The QCL structure presented in Ref. [4]. 29

2.5 Comparison of bandstructures solved by (a) ST solver and (b) Sequal solver for the structure given in Ref. [4]. 30

3.1 Cross section diagram of a ridge waveguide mid-IR QCL 34

3.2 Schematic diagram of ridge waveguide QCL fabrication process . . 35

3.3 Optical microscopic pictures of (a) Z35 and (b) Z45 devices' facets. (c) Top view of the array of Z35 waveguide ridges, two of which are wire-bonded. 37

3.4 Simulation results of fundamental optical mode distribution in Z35 and Z45 ridge waveguides with the red arrow indicating E field direction. The effective refractive index n and waveguide loss α_w are also indicated. (a) $\lambda = 9$ μm, width = 31.8 μm; (b) $\lambda = 4$ μm, width = 16.7 μm. Parameters used in the simulation: refractive index of Au is 10.21+50.2i at $\sim$9 μm and 2.6+24.6i at $\sim$4 μm[31]. Refractive index of noncrystalline Si_3N_4 is 1.8+0.2i at $\sim$9 μm and SiO_2 is 1.38+1.38i at $\sim$4 μm [32]. 38

4.1 Top view of a Z35 device successfully mounted on a copper submount. 41

4.2 Schematic illustration of LIV measurement setup. 42

4.3 (a) LIV measured for a 9 μm device Z353, for which the waveguide length is 1.2 mm, ridge width is 30.3 μm. (b) J_{th} vs. T with T_0 extracted. 43

4.4 (a) LIV measured for a 4 μm device Z451, for which the waveguide length is 2.1 mm, ridge width is 14 μm. (b) J_{th} vs. T with T_0 extracted. 44

4.5 Characteristic T_0 extracted for three 9 μm devices of different lengths cleaved from the same waveguide. The ridge width is 30.3 μm. Cavity length for Z352, Z353, Z354 are 1.8 mm, 1.2 mm, 0.8 mm. . . 45

4.6 (a) J_{th} vs. inverse cavity length and (b) inverse slope efficiency vs. cavity length under different temperature for three 9 μm QCL devices with 30.3 μm wide ridge. (c) Extracted differential modal gain vs. temperature, with its fitting curve (red). (d) Extracted waveguide loss vs. temperature. $R_1 = R_2 = 0.275$ with $n = 0.312$. 47

4.7 (a) Transparency current density J_{tr} vs. temperature extracted for Z35 device of 30.3 μm wide ridge based on LIVs for Z352, Z353 and Z354, as well as the fitting curve (red). (b) The percentage of J_{tr} in J_{th} for Z352, Z353 and Z354 of different cavity length. 48

4.8 Schematic illustration of (a) QCL lasing spectra measurement setup and (b) EL spectra measurement setup. 50

4.9 Lasing spectra for Z353 at RT under different bias. Z353 is 1.2 mm long and 30.3 μm wide. The spectral resolution is 0.125 cm^{-1} . . 50

4.10 (a) The 9 μm disk devices (diameter=208 μm) cut in half for EL measurement at RT. (b) EL spectra and fitting results for the 9 μm mesa piece at RT pulsed at 80 KHz with 200 ns pulse width. The spectral resolution is 16 cm^{-1}. 51

4.11 (a) Schematic of beam pattern measurement coordinates. (b) The beam pattern measurement result for Z354 at 11.33 V bias and RT. 52

4.12 E-plane cut (a) and H-plane cut (b) of the 2D beam pattern for Z354 fitted with Gaussian function. 52

List of Tables

2.1 Comparison of eigen-energies solved by the ST solver and the values given in [26] for the same structure. 27

2.2 Comparison of eigen-energies solved by Sequal solver and ST solver for the structure given in Ref. [4]. 31

2.3 Comparison of LO lifetimes solved by the ST solver and the Sequal solver for the structure given in Ref. [4]. 31

3.1 Comparison of design widths and actual widths for Z35 and Z45 devices. 36

3.2 Simulation results of waveguide loss α_w for zero doping and a usual doping [33] in the active region, and confinement factor Γ (zero doping) for Z35 devices of four different ridge widths at 9 μm wavelength. 39

Acknowledgments

I would like to thank my advisor, Professor Benjamin Williams, for his guidance and support throughout this work. I would also like to thank my lab mates, especially Dr. Zhijun Liu who gave me lots of valuable advices and help, for their help and willingness for discussion. This project is in cooperation with Pranalytica Inc. which I want to thank for their good partnership. I am also very grateful for my family and friends for encouraging me as I pursue graduate school.

Vita

2009-2011	Undergraduate Research Assistant for Professor Daoxin Dai, Department of Optical Engineering, Zhejiang University.
2011	B.S. in Optical Engineering, Hangzhou, China, Zhejiang University.
2011-present	Graduate Research Assistant, Electrical Engineering Department, UCLA.

Publications

"Terahertz Properties of Topological Insulators." Zhijun Liu , Luyao Xu , Benjamin Williams, Xufeng Kou, Kang L. Wang. Focus Center Research Program, P059893, 2011.

CHAPTER 1

Introduction

Presently, semiconductor lasers are an important light source for common appliances, especially the widely-used double heterostructure lasers. Double heterostructure lasers have been commercialized for wavelengths from the visible blue to the invisible near infrared, up to about 1.6 μm [1]. But the scientifically and technologically interesting mid-infared (mid-IR) range (2-20 μm) is hard to approach to by the conventional semiconductor lasers due to the limitation of narrow natural bandgap that mid-IR light emission requires.

The invention of quantum cascade lasers (QCLs) [2] largely satisfies the increasing need for compact, high-performance, room-temperature, and reliable mid-IR laser sources. QCLs are electrically-injected semiconductor lasers based on intersubband electron transitions, instead of conventional electron-hole recombination. Due to its engineered-bandstructure nature, a QCL can be designed to emit essentially any wavelength within the mid-IR spectrum. Even for the far IR, which is also referred to as terahertz range loosely defined as 300 GHz to 10 THz, or the wavelengths from 30 μm to 1000 μm, a wide range of it (600 GHz to 5 THz approximately) can reached by a QCL [1, 3, 4, 5]. The progression of QCLs research in the past 20 years not only accelerates various mid-IR applications, but also exploits the scientific frontier of physics by design [6].

This chapter will review the application and sources of mid-IR light. An overview of mid-IR QCLs will be presented, including bandstructure and optical gain, waveguide and loss, as well as several important performance parameters.

1.1 Mid-infrared applications and sources

Mid-infrared radiation has found a wide range of applications in, for example, biological and medical diagnostics, chemical sensing, atmospheric and environmental monitoring, free-space communication and military countermeasures [7]. Mid-IR spectrum is often called the molecular-fingerprint region [8], in which the most identifiable molecules absorb and radiate because the associated vibrorotational transitions have their energy within the mid-IR photon energy range, as shown in Fig. 1.1. Thus the mid-IR spectroscopy provides a sensitive tool to examine the chemical makeup of molecule. The two wavelength regions (3-5 μm and 8-13 μm) are atmosphere-transparent due to lack of water vapor absoprtion, thus allowing the highly sensitive measurement of environmental and toxic gases or vapors [1]. IR countermeasures are standard equipment for military aircraft. It is designed to prevent a heat- or plume-seeking missile from reaching its target by confusing the missile's target acquisition system using IR light sources [9]. Compact size and light weight are favorable features for IR sources used in countermeasures systems.

Even though QCLs turn out to be nearly ideal mid-IR laser source, it is noted that there are several other types of mid-IR sources that can generate laser-like beams. Lead salt lasers are typical semiconductor lasers based on ternary or quaternary compounds with shrinking bandgap below 0.5 eV to lase in the mid-IR range. But the continuous wave (CW) operation normally needs cryogenic condition due to the low thermal conductance of lead salts and the comparative softness of this material affects the stability of lead salt lasers [10]. A few types of transition metal doped binary and ternary chalcogenides crystal solid-state lasers emit in the mid-IR region, such as chromium-doped zinc selenide lasers which emit over 1.9-3.1 μm [11]. The choice of laser crystals and glasses is limited to those with low phonon energies that weakly interact with mid-IR light. The carbon

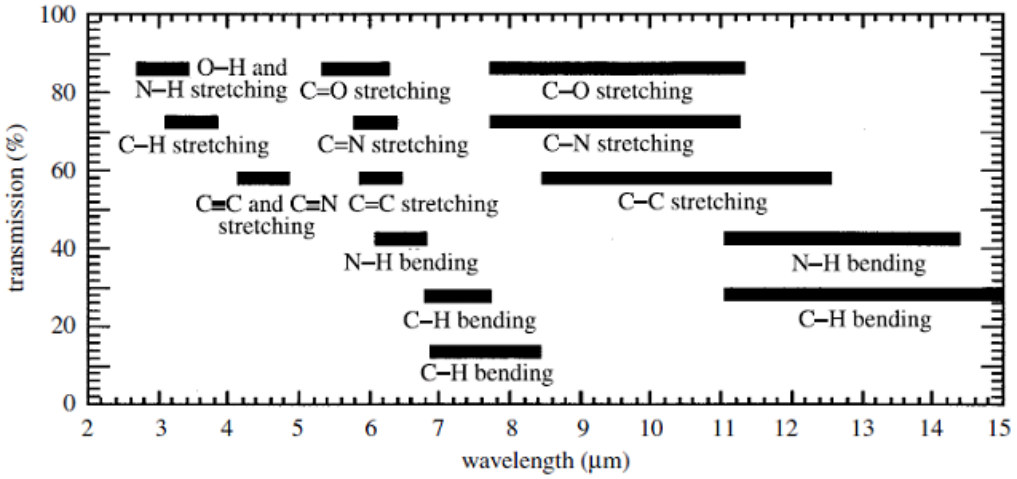

Figure 1.1: Simple correlations of various group molecular vibrations. Figure from [8].

dioxide (CO_2) laser, the earliest gas lasers to be developed [12], produces highest-power continuous wave centering around 9.4 μm and 10.6 μm. Because of the high power levels available, CO_2 lasers are frequently used in industrial applications like cutting and welding. There are other sources based on difference frequency generation and optical parametric oscillators [7].

1.2 Overview of mid-infrared quantum cascade lasers

A QCL is a semiconductor injection laser based on intersubband transitions in multiple-quantum-well structures. The light emitting process in QCLs only involves electrons, and is realized by forcing electrons to undergo quantum jumps between the discrete energy levels created in the quantum wells (QWs) structure. An electron stays in the conduction band after emitting a photon and is recycled by being injected into the next identical active period, where it emits another photon. This process goes on in every repeating module, leading to the cascade effect. This is a radically different operation mechanism from conven-

tional semiconductor lasers which rely on the electron-hole recombination cross the bandgap. The design of alternating wells and barriers allows flexibility for a QCL's emission wavelength to be tailored over a wide range. The high quality heterostructure growth technology leads to mature established material systems like InGaAs/AlInAs alloys on InP and GaAs/AlGaAs on GaAs, on which the majority of QCLs are based.

The concept of light amplification in intersubband transitions was first proposed by Kazarinov and Suris in 1971 in a seminal paper [13]. But the progression from this preliminary concept to the demonstration of the first QCL took more than 20 years. The first QCL emitting at 4.3 μm was experimentally demonstrated at Bell Labs in 1994 by Faist, Capasso, Sivco, Sirtori, Hutchinson, and Cho [2]. This prototype device operated only in pulsed mode at maximum temperature of 90 K with the peak power below 10 mW and the wall-plug efficiency (WPE) less than 0.15%. But the rapid development in this field has led to many important achievements as Fig. 1.2 shows. As an increasing number of mid-IR QCLs applications are proposed, the need for improving WPE of mid-IR QCLs is growing and becoming a recent research focus [14]. Most recent achievements in WPE include CW room-temperature operation with WPE up to 21% with a maximum output power of 5.1 W [15] and a record WPE of more than 50% at 40 K in pulsed operation [16].

1.2.1 Bandstructure and optical gain

The optical gain in QCLs is provided by the intersubband radiative transition between the upper and lower lasing levels in conjunction with the electron population inversion achieved via scattering and tunneling processes. Fig. 1.3 illustrates a typical scheme and design of mid-IR QCL. The deep-etched ridge waveguide structure is widely used for mid-IR QCLs. The front and rear cleaved facets are reflective, forming a Fabry-Perot cavity to provide optical feedback. The laser

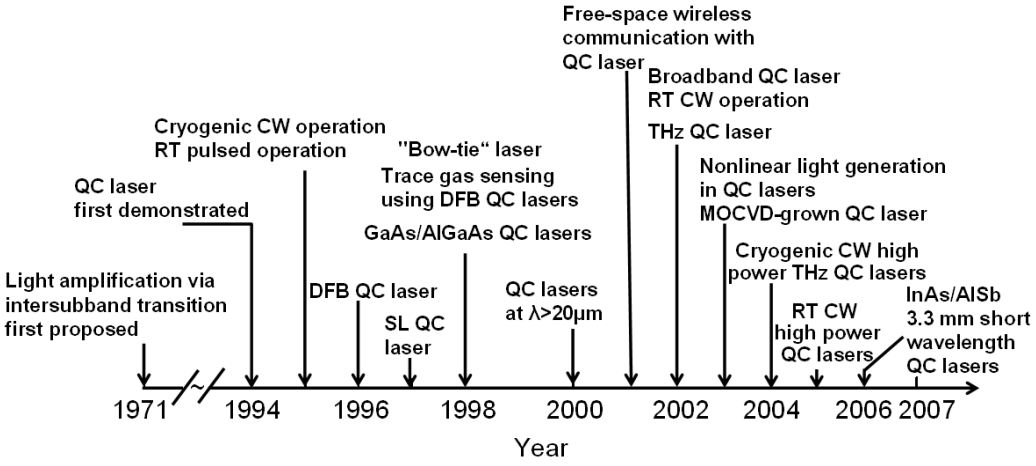

Figure 1.2: Schematic timeline of major developments in QCLs. Figure from [17].

active core is presented in red in Fig. 1.3 (a), and its microscopic structure is shown in Fig. 1.3 (b). The active core is composed of typically several tens of periods, each made up by alternating wells and barriers. The total number of wells and barriers is often 500-1000 [14]. The electron wavefunctions within these potential wells and barriers in the materials' conduction can be solved from the one-dimensional effective mass Schrödinger equation, which are plotted in Fig. 1.3 (c).

The "active region" refers to the part of active core where the radiative transitions occur, and the "injector" refers to the transport region between two adjacent active regions. The laser transition occurs between level 3 and level 2 as shown in Fig. 1.3 (c). The depopulation process is via the fast resonant longitudinal optical (LO) phonon emission process from level 2 to level 1. This condition requires the energy spacing betwen these two levels to be close to the LO phonon energy ($\sim$34 meV in InP material system) to achieve a short value of τ_{21} (in the order of subpicosecond usually). There might be other levels other than level 1 affecting τ_2 through LO phonon scattering or tunneling processes. The lower lasing level lifetime τ_2 is much smaller than the upper lasing level lifetime τ_3, which makes

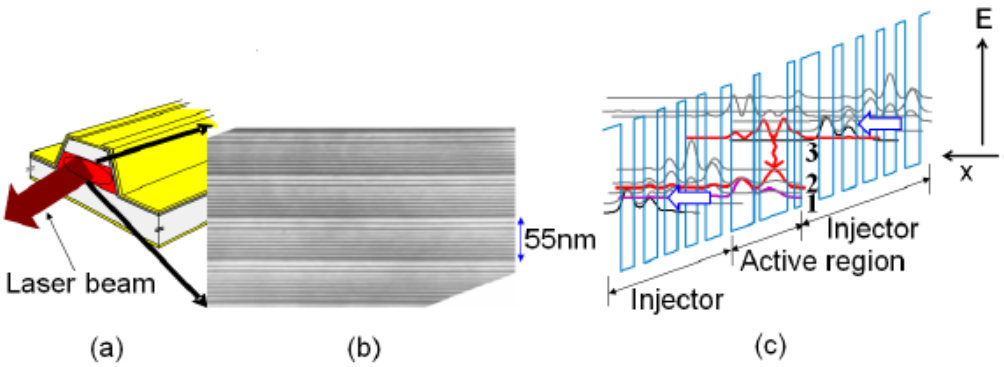

Figure 1.3: (a) Schematic of a deep-etched, ridge waveguide QCL. The brown arrow indicates the laser emission. (b) A Transimission Electron Microscopy (TEM) image of the active core of a QCL. The dark layers are the $In_{0.52}Al_{0.48}As$ barriers, and the bright layers are the $In_{0.53}Ga_{0.47}As$ wells. (c) Conduction band diagram of one active region sandwiched by two injectors and the moduli squared of relevant wavefunctions. Figure from [17]

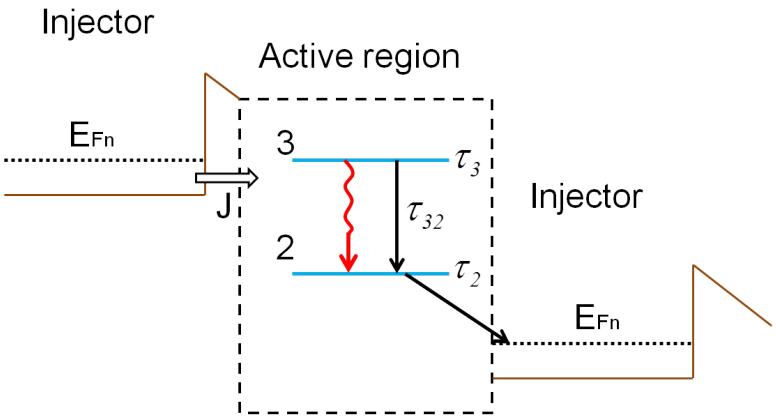

Figure 1.4: A three-level laser system model for QCLs.

it possible to build up a population inversion between the two levels. However, it is worth mentioning that the small value of τ_{21} is sometimes misleading, because ultimately the population in level 1 is extracted to the next injector region through a tunneling process. The relatively long tunneling time will limit the ratio of population n_2/n_3, which is called the electron extraction bottleneck [4].

The optical gain in QCLs can be modeled using conventional rate equations for a three-level laser system as represented in Fig. 1.4. The level 3 is the upper lasing level and the level 2 is the lower lasing level. The rate equations for these two electron energy levels are:

$$\frac{dn_3}{dt} = \eta\frac{J}{e} - \frac{n_3}{\tau_3} - g_c S(n_3 - n_2) \tag{1.1}$$

$$\frac{dn_2}{dt} = (1-\eta)\frac{J}{e} + \frac{n_3}{\tau_{32}} - \frac{n_2}{\tau_2} + g_c S(n_3 - n_2) \tag{1.2}$$

$$\frac{dS}{dt} = \frac{c}{n}\left[\frac{1}{L_p}\Gamma g_c S(n_3 - n_2) - \alpha S\right] \tag{1.3}$$

The notation used above is summarized below.

n_3 and n_2: Sheet density of electrons in state 3, 2 (cm^{-2}).

η: Injection efficiency describing the percentage of the electrons that are injected to the upper lasing level with respect to the lower lasing level.

J: Pumping current density (Acm^{-2}).

e: Electron charge (C).

g_c: Peak gain cross section (cm^2).

S: Photon flux density ($\mathrm{s}^{-1}\mathrm{cm}^{-2}$).

τ_3 and τ_2: Electron lifetime in state 3, 2 (s).

τ_{32}: The nonradiative relaxation time from state 3 to state 2 (s).

c: Light velocity in vacuum (cm/s).

n: Refractive index of the medium.

α: Total optical loss (cm^{-1}).

L_p: Length of one period of the active core (cm).

Γ: The optical confinement factor describing the overlapping between the gain medium and the optical mode.

The bulk population density inversion between state 3 and state 2 in the steady state is obtained from Eq. 1.1-1.3 as

$$\Delta N = \frac{n_3 - n_2}{L_p} = \frac{1}{L_p} \frac{\eta \frac{J}{e} \tau_{up} - (1-\eta)\frac{J}{e}\tau_2}{1 + (\tau_2 + \tau_{up})(g_c S)} \tag{1.4}$$

where $\tau_{up} = \tau_3(1 - \frac{\tau_2}{\tau_{32}})$ is the effective upper lasing level lifetime. Below the laser threshold condition, the photon flux density S is negligibly small. Thus the population inversion can be simplified as

$$\Delta N = \frac{J}{eL_p} [\eta \tau_{up} - (1-\eta)\tau_2] \tag{1.5}$$

The population inversion obtained in Eq. 1.5 describes its linear relationship with the injection current density, which is just a rough approximation that neglects the thermal backfilling effect rising with increased temperature.

Based on Fermi's golden rule and assuming a Lorentzian lineshape for the stimulated transition, the peak gain cross section g_c takes the form of [18]

$$g_c = \frac{e^2 f_{32}}{2\pi m^* c n \epsilon_0 \Delta \upsilon} \tag{1.6}$$

where f_{32} is the scaled oscillator strength, $\Delta\upsilon$ is the full-width half maximum (FWHM) linewidth of the laser transition, ϵ_0 is the vacuum electric permittivity, and m^* is the electron effective mass of the well material since the electron spends the majority of its time there.

The peak bulk gain can be written as

$$g(\upsilon_0) = \Delta N g_c = \frac{J}{eL_p} [\eta \tau_{up} - (1-\eta)\tau_2] \frac{e^2 f_{32}}{2\pi m^* c n \epsilon_0 \Delta \upsilon} \tag{1.7}$$

The lifetimes of level 3 and 2 are dominated by nonradiative LO phonon scattering. To improve the optical gain in QCLs, the alternating quantum wells and

barriers are designed to make the upper lasing level lifetime τ_3 much longer than the lower level lifetime τ_2 to achieve the population inversion, and to increase the oscillator strength f_{32} by designing the wavefunctions of the two lasing states. The design of a QCL is a sophisticated work that needs the accurate numerical solution to one-dimensional Schrödinger equation based on the one-band effective mass envelope function approximation [18]. The details of this calculation are presented in Chapter 2.

Adjacent to the active region is the injector region. Part of the injector is often doped with Si atoms to supply sufficient electrons to the active region as an electron reservoir. The injector also provides a transport channel for the electrons residing in the active region to travel down to the upper lasing level of the next active region via LO phonon emission and resonant tunneling processes. The energy separation between the lower lasing level and the ground level in the injector in each period also suppresses the thermal excitation of electrons to the lower lasing level, a process known as thermal backfilling, sustaining the population inversion. The electron injection process in the injector is complex, which includes many intersubband scattering processes, such as LO phonon scattering, electron-electron scattering, and interface roughness scattering [4].

1.2.2 Waveguide and loss

The laser emission is turned on only when the threshold condition is met, which requires the modal gain to reach the loss as represented in Eq. 1.8. The modal gain is the effective gain experienced by the lasing optical mode which has an overlapping with the gain medium. Eq. 1.3 contains the information of this threshold condition.

$$\Gamma g(\upsilon_0) - \alpha = 0 \tag{1.8}$$

The waveguide loss α contains two parts - mirror loss α_m and waveguide loss

α_w. A typical QCL is constructed based on Fabry-Perot cavity formed by two parallel, cleaved semiconductor facets with a reflectivity R of

$$R = \left(\frac{(n-1)}{(n+1)}\right)^2 \tag{1.9}$$

where n is the effective refractive index of the lasing mode. The mirror loss is given by

$$\alpha_m = \frac{1}{2L} ln(R_1 R_2) \tag{1.10}$$

where L is the cavity length, and R_1 and R_2 are the reflectivity of the two facets.

The waveguide loss is mainly induced by free carrier absorption in the QCL's active core and cladding layers. The free carrier loss is typically calculated from the bulk Drude model which gives the frequency dependent permittivity as [18]

$$\epsilon(\omega) = \epsilon_{core}\left(1 - \frac{{\omega_p}^2\tau^2}{1+(\omega\tau)^2} + i\frac{{\omega_p}^2\tau}{\omega(1+(\omega\tau)^2)}\right) \tag{1.11}$$

where ϵ_{core} is the core permittivity excluding free carrier contributions, and

$$\omega_p^2 = \frac{ne^2}{m^*\epsilon_{core}} \tag{1.12}$$

defines the plasma frequency for the active core material. n is the free carrier density, m^* is the effective mass, and τ is the momentum relaxation time or the Drude scattering time.

For mid-IR QCLs, the Drude scattering time is generally long enough so that $\omega\tau \gg 1$ and the free carrier loss is given by [18]

$$\alpha_{fc} = \frac{{\omega_p}^2}{\omega^2}\frac{1}{c\tau}\sqrt{\frac{\epsilon_{core}}{\epsilon_0}} = \frac{ne^2\lambda^2}{4\pi^2 m^* c^3 \tau \epsilon_0}\sqrt{\frac{\epsilon_0}{\epsilon_{core}}} \tag{1.13}$$

from which it is observed that the free carrier loss increases with the lasing wavelength, doping density and Drude scattering rate.

The mirror loss can be adjusted to tune the optical out-coupling efficiency, which can maximize the WPE of QCLs [19]. The waveguide loss is expected to be minimized to lower the threshold current and improve the lasers' efficiency.

1.2.3 Performance parameters

The progress of mid-IR QCLs studies is often marked by the improvement of the key performance parameters. Lower threshold current, higher slope efficiency, and higher wall-pluge efficiency (WPE) are always desired for QCL designs.

1.2.3.1 Threshold current

The threshold current is given by the threshold condition which sets the modal gain equal to the loss as shown in Eq. 1.8. QCLs only start to lase when the driving current density is above the threshold. Below the threshold, the peak bulk gain $g(\upsilon_0)$ can be written as

$$g(\upsilon_0) = \frac{J}{eL_p}\left[\eta\tau_{up} - (1-\eta)\tau_2\right] g_c = g_J J \tag{1.14}$$

where g_c is given in Eq. 1.6, and $g_J = \frac{g(\upsilon_0)}{J}$ is defined as the differential bulk gain. The threshold current is given by

$$J_{th} = \frac{\alpha_m + \alpha_w}{\Gamma g_J} = \frac{e}{\eta\tau_{up} - (1-\eta)\tau_2}\frac{\alpha_m + \alpha_w}{L_p \Gamma g_c} \tag{1.15}$$

where Γg_J is defined as the differential modal gain.

A more complete expression for J_{th} should takes into account the transparency current that induced by the thermal backfilling effect.

$$J_{th} = \frac{e}{\eta\tau_{up} - (1-\eta)\tau_2}\left[\frac{\alpha_m + \alpha_w}{L_p \Gamma g_c} + \Delta n_{therm}\right] = J_{tr} + \frac{1}{\Gamma g_J}(\alpha_w + \alpha_m) \tag{1.16}$$

where J_{tr} is defined as transparency current density, and Δn_{therm} is the thermal backfilling sheet density of the lower laser level. A simple approximation of Δn_{therm} is given by

$$\Delta n_{therm} = n_s exp(\frac{-\Delta_{inj}}{kT}) \tag{1.17}$$

where n_s is the sheet doping density period, k is the Boltzmann constant, T is the electron temperature and Δ_{inj} is the voltage defect that defines the energy

separation between the ground injector level and the lower laser level in one period. A more refined model for thermal backfilling density is presented in [20].

1.2.3.2 Slope efficiency

The slope efficiency measures how much optical power is generated with an additional unit of current injected into a QCL above the threshold current. It has the expression of [18]

$$\frac{dP}{dI} = \frac{\hbar\omega}{e} N_{mod} \frac{\alpha_m}{\alpha_m + \alpha_w} \left[\frac{\eta\tau_{up} - (1-\eta)\tau_2}{\tau_2 + \tau_{up}} \right] \tag{1.18}$$

where N_{mod} is the number of active core stages. The quantity in brackets defines the internal efficiency η_i. Although η_i is smaller than unity, the essential feature of cascade lasers is reflected in N_{mod} which allows the differential quantum efficiency to be greater than unity. Physically it originates in the fact than a single injected electron can emit several tens of photons [18].

1.2.3.3 Wall-plug efficiency

The wall-plug efficiency (WPE) defines the ratio between the optical power generated by a QCL and the total electrical power consumed by it. It has been a crucial parameter that impacts the wide application of mid-IR QCLs because a low WPE puts heavy demands on power supply and heat dissipation system design [14]. The WPE η_{wp} can be expressed as

$$\eta_{wp} = \frac{I - I_{th}}{I} \frac{\hbar\omega}{\hbar\omega + \Delta_{inj}} N_{mod} \frac{\alpha_m}{\alpha_m + \alpha_w} \left[\frac{\eta\tau_{up} - (1-\eta)\tau_2}{\tau_2 + \tau_{up}} \right] \tag{1.19}$$

The WPE is a complicated parameter that depends on many factors such as the operation temperature, the quantum structure design, the waveguide length and loss [14]. The strategies to improve WPE need to make trade-offs between various design parameters. Fig. 1.5 shows a plot of WPE reported over time for both pulsed and CW operation.

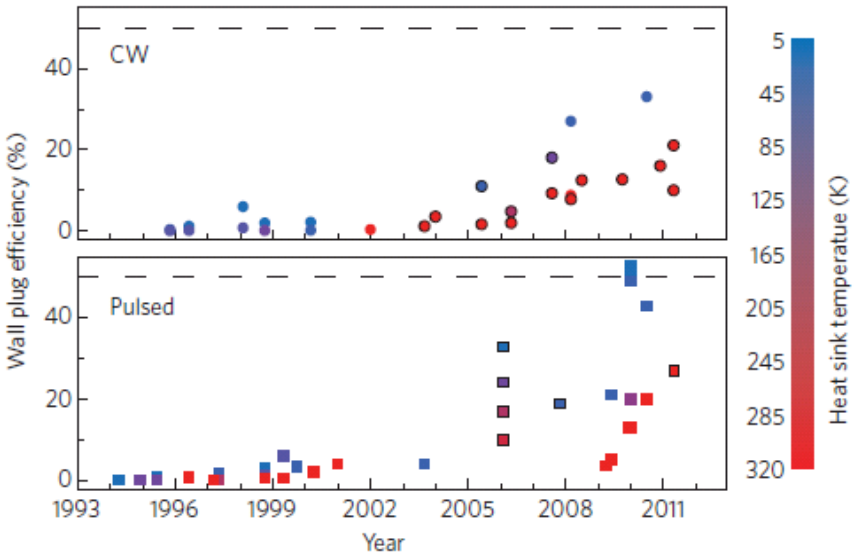

Figure 1.5: Total WPE of selected lasers from the literature at various heat sink temperatures for pulsed and CW operation. Figure from [14].

1.3 Thesis overview

This thesis is organized as follows: Chapter 2 details the theoretical fundamentals essential to the design of a QCL and presents a numerical method for QCL bandstructure calculation, radiative and non-radiative transition rates. Chapter 3 introduces the structure and simulation of ridge waveguide for mid-IR QCLs, and its micro-fabrication procedures as well as results; Chapter 4 summarizes and analyzes all testing and characterization work for mid-IR QCLs, leading to a comprehensive knowledge of devices' performance. Chapter 5 makes concluding remarks.

CHAPTER 2

QCL bandstructure modeling and solver

2.1 Introduction

In this chapter the fundamental theories essential to the design of mid-IR QCLs are reviewed, following which a numerical solver for QCL bandstructure calculation is introduced, implemented and verified. To avoid the complexity added by the material system like strain effect, my focus will be on a lattice-matched material system $In_{0.53}Ga_{0.47}As/In_{0.52}Al_{0.48}As$, which is a typical choice for mid-IR QCLs including the first demonstration of QCL [2]. The conduction band offset is around 520 meV [21]. Effects of nonparabolicity must be considered due to the relatively high energy of electrons above the conduction band edge of electrons [22].

2.2 Intersubband laser theory

QCLs rely on electronic transitions between conduction band states, which are referred to as subbands that arise from size quantization in the growth direction in multiple heterostructures. These transitions are denoted intersubband transitions. As shown in Fig. 2.1, the initial and final subband states have the same E-k curvature if nonparabolicity is neglected, and therefore the joint density of state lineshape is very sharp, giving rise to an atomic-like transition. The gain is achieved with the sustained population inversion and the gain linewidth depends only indirectly on temperature through collision processes [23]. In contrast, the interband transition gain requires the carrier injection to be high enough to have

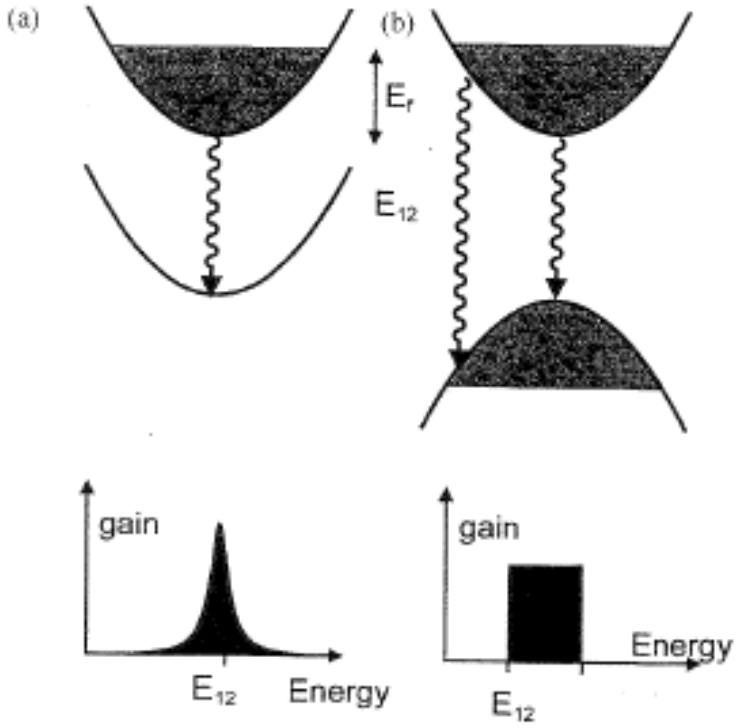

Figure 2.1: Comparison between an intersubband transition (a) and an interband transition in a quantum well. Figure from [23].

the quasi-Fermi levels separation exceeding the bandgap [24]. The gain linewidth determined by the bandgap and that separation is quite broad (of the order of the thermal energy kT) [23] and increases with pumping .

2.2.1 Electronic states in quantum wells

The multiple heterostructures are atomically abrupt layers composed of materials of different bandgaps like $In_{0.53}Ga_{0.47}As/In_{0.52}Al_{0.48}As$ material system. At each interface, there is a sharp discontinuity in the band energies called band offset. The conduction band offset determines the QW's depth. To solve the quantized electron energy and states in the growth direction denoted as z, the effective mass theorem in the envelope function approximation is used based on the thesis of

Williams [18].

The wavefunction for the electron is given by

$$\Psi(\mathbf{r}) = F(\mathbf{r})U_{n,0}(\mathbf{r}) \tag{2.1}$$

where $U_{n,0}(\mathbf{r})$ is the Bloch state wavefunction at the band minimum and $F(\mathbf{r})$ is the envelope function satisfying the effective mass equation as below

$$\left[-\frac{\hbar\nabla_{\parallel}^2}{2m^*(z)} - \frac{\hbar^2}{2}\frac{\partial}{\partial z}\frac{1}{m^*(z)}\frac{\partial}{\partial z} + E_c(z)\right]F(\mathbf{r}) = EF(\mathbf{r}) \tag{2.2}$$

The Γ-point effective mass $m^*(z)$ is assigned to describe the conduction band curvature of each constituent material along the direction z. The potential $E_c(z)$ represents the conduction band edge profile along z, with any externally applied bias field and the local variation due to space charge. $\nabla_{\parallel}$ is the in-plane differential operator. The solution to Eq. 2.2 is given by

$$F(\mathbf{r}) = \frac{1}{\sqrt{S_{\parallel}}}e^{i\mathbf{k}_{\parallel}\cdot\mathbf{r}_{\parallel}}\psi_n(\mathbf{k}_{\parallel}, z) \tag{2.3}$$

where $\psi_n(\mathbf{k}_{\parallel}, z)$ should satisfy

$$\left[-\frac{\hbar^2}{2}\frac{\partial}{\partial z}\frac{1}{m^*(z)}\frac{\partial}{\partial z} + E_c(z) + \frac{\hbar\mathbf{k}_{\parallel}^2}{2m^*(z)}\right]\psi_n(\mathbf{k}_{\parallel}, z) = E_n\psi_n(\mathbf{k}_{\parallel}, z) \tag{2.4}$$

and $\mathbf{k}_{\parallel}$ is the in-plane wavevector, n is the subband index, and $S_{\parallel}$ is the normalization area.

Usually we can replace $\frac{\hbar\mathbf{k}_{\parallel}^2}{2m^*(z)}$ to $\frac{\hbar\mathbf{k}_{\parallel}^2}{2m^*}$ with m^* to be the well material effective mass. As long as the in-plane energy is modest compared to the barrier height, this approximation won't introduce too much difference. Therefore we arrive at the one-dimensional (1D) Schrödinger equation in the multiple QWs structure

$$\left[-\frac{\hbar^2}{2}\frac{\partial}{\partial z}\frac{1}{m^*(z)}\frac{\partial}{\partial z} + E_c(z)\right]\psi_n(z) = E_n\psi_n(z) \tag{2.5}$$

and the total energy is given by

$$E = E_n + \frac{\hbar\mathbf{k}_{\parallel}^2}{2m^*} \tag{2.6}$$

There are two additional factors that might affect the accuracy of electronic states solved by Eq. 2.5: space-charge effect and nonparabolicity. Population of electrons in different electronic states introduce space charge which build up an electrostatic potential that affects the conduction band profile $E_c(z)$. The electrostatic potential can be solved using the Poisson equation [25]. The Poisson and Schrödinger equations are iteratively solved to obtain a self-consistent solution for E_n. But due to the low doping and thus low electron density in the majority of QCL designs, the space-charge effect is insignificant and self-consistent solution is unnecessary. So it is not considered in this work.

Nonparabolicity, however, is taken into account in all the calculations in this thesis. The occupation of electrons in subband states higher above the conduction band edge leads to the deviation from the parabolic E-k relation due to the interaction between the conduction band and the valence band [22]. This interaction gets enhanced for electrons occupying higher energy states above the conduction band edge, which makes nonparabolicity effect more noticeable in mid-IR QCLs than terahertz ones. Based on the empirical two-band model [26], the energy-dependent conduction band effective mass is incorporated into Eq. 2.5 to incorporate the nonparabolicity effect. The energy dependence of the effective mass is given by [27]

$$m(E) = m^* \left[1 + \frac{2m^*\gamma(E - E_c)}{\hbar^2}\right] \tag{2.7}$$

where γ is the nonparabolicity parameter, and E_c is the conduction band profile with or without the external bias. γ is usually given for the well material in QCLs, while γ for the barrier material is found by the following relation [26] with the effective mass values for well and barrier materials given:

$$\frac{\gamma_w}{\gamma_b} = \left(\frac{m_b^*}{m_w^*}\right)^2 \tag{2.8}$$

The incorporation of nonparabolicity implies that the electron wavefunction contains a component from the "fictitious" valence band according to the empirical

two-band model [27], which is given by

$$\psi_n^v(z) = -\frac{m^*\sqrt{\gamma}}{m(E,z)}\frac{d\psi_n(z)}{dz} \tag{2.9}$$

The two components $\psi_n(z)$ and $\psi_n^v(z)$ constitute the electron wavefunction. However, we are only interested the intersubband transition that happens between the conduction band states in QCLs. Therefore only the conduction band wavefunction component $\psi_n(z)$ are used to calculate the intersubband transition rate in this thesis. The effect of nonparabolicity on the transition rate shows up as a tiny reduction of the amplitude of $\psi_n(z)$.

2.2.2 Intersubband radiative transitions

The stimulated emission of photons by the intersubband radiation transition in the active region provides the optical gain for a QCL. The radiative transition rate, either spontaneous or stimulated, is given by Fermi's golden rule [18]

$$W_{i\to f} = \frac{2\pi}{\hbar}\left|\left\langle f, n_{\mathbf{q},\sigma}\left|H^{/\prime}\right|i, m_{\mathbf{q},\sigma}\right\rangle\right|^2 \delta(E_f(\mathbf{k}_f) - E_i(\mathbf{k}_i) \mp \hbar\omega_{\mathbf{q}}) \tag{2.10}$$

where

$$H^{'} = -\frac{e}{m^*}\sqrt{\frac{\hbar}{2\epsilon\omega_{\mathbf{q}}V}}\hat{\mathbf{e}}_{\mathbf{q},\sigma}\left[a_{\mathbf{q},\sigma}e^{i\mathbf{q}\cdot\mathbf{r}} + a^{\dagger}_{\mathbf{q},\sigma}e^{-i\mathbf{q}\cdot\mathbf{r}}\right]\cdot\mathbf{p} \tag{2.11}$$

is the interaction Hamiltonian for a harmonic electro-magnetic field interaction. $a_{\mathbf{q},\sigma}$ and $a^{\dagger}_{\mathbf{q},\sigma}$ are the raising and the lowering operators. The initial and final states $\left|i, m_{\mathbf{q}/,\sigma}\right\rangle$ and $|f, n_{\mathbf{q},\sigma}\rangle$ are product states of the electron conduction band envelope function eigenstates i, f and the photon eigenstates with n and m photons in each mode given by the photon wavevector $\mathbf{q}$ at frequency $\omega_{\mathbf{q}}$, and the polarization state described by $\sigma = 1, 2$. ϵ is the permittivity of the material where this transition happens. V is the volume of the cavity, and $\hat{\mathbf{e}}_{\mathbf{q},\sigma}$ is the polarization vector. m^* is taken to be the effective mass of the well material since the electron spends most of its time there.

After inserting the electron wavefunctions in forms of Eq. 2.3 in to Eq. 2.10 and carrying out the calculation, we obtain the following spontaneous and stimulated transitions rates [18]:

$$W^{(sp)}_{i\to f/mode} = \frac{\pi e^2 \omega_{\mathbf{q}}}{\epsilon V} \left|\hat{e}_{\mathbf{q},\sigma} \cdot \hat{z}\right|^2 \left|z_{i\to f}\right|^2 \delta(E_f - E_i + \hbar\omega_{\mathbf{q}}) \tag{2.12}$$

$$W^{(st)}_{i\to f/mode} = \frac{\pi e^2 \omega_{\mathbf{q}}}{\epsilon V} \left|\hat{e}_{\mathbf{q},\sigma} \cdot \hat{z}\right|^2 \left|z_{i\to f}\right|^2 \delta(E_f - E_i + \hbar\omega_{\mathbf{q}}) m_{\mathbf{q},\sigma} \tag{2.13}$$

where $m_{\mathbf{q},\sigma}$ is the number of photons with wavevector $\mathbf{q}$ in the polarization mode σ.

Summing over all the photon modes and polarizations in the cavity leads to the total spontaneous emission rate:

$$W^{(sp)}_{i\to f} = \frac{e^2 n \omega_0^2}{6\pi m^* \epsilon_0 c^3} f_{i\to f} \tag{2.14}$$

where n is the index of refraction at the frequency $\omega_0 = \left|E_i - E_f\right|/\hbar$, c is the speed of light in vacuum, and $f_{i\to f}$ is the dipole matrix element, or the scaled oscillator strength

$$f_{i\to f} = \frac{m^*}{m_0} f_{i\to f,unscaled} = \frac{2m^*(E_i - E_f)\left|z_{i\to f}\right|^2}{\hbar^2} \tag{2.15}$$

The spontaneous lifetime is

$$\tau^{(sp)}_{i\to f} = \frac{1}{W^{(sp)}_{i\to f}} \tag{2.16}$$

The total simulated emission rate is obtained in the same way by representing $m_{\mathbf{q},\sigma}$ as

$$m_{\mathbf{q},\sigma}(\nu) = \frac{\rho_I}{\rho(\nu)} = \frac{\lambda^2}{8\pi n^2 h\nu} I(\nu) \tag{2.17}$$

where $\rho_I = \frac{I(\nu)n}{h\nu c}$ is the total number of photons per unit volume with $I(\nu)$ defining the incident wave intensity. $\rho(\nu) = \frac{8\pi n^3}{c\lambda^2}$ is mode density per unit frequency [28]. c and λ are the velocity and wavelength of incident electromagnetic

wave in vacuum that corresponds to frequency ν. n is the effective refractive index of the active medium.

Since $m_{\mathbf{q},\sigma}(\nu)$ is independent of the wavevector $\mathbf{q}$, summing Eq. 2.13 over all electromagnetic modes leads to the total simulated emission rate as

$$W_{i\to f}^{(st)} = 3^* W_{i\to f}^{(sp)} \cdot m_{\mathbf{q},\sigma} \cdot g(\nu) = \frac{3^*\lambda^2}{8\pi n^2 h\nu \tau_{i\to f}^{(sp)}} I(\nu) g(\nu) \tag{2.18}$$

where 3^* is added due to the fact that all the electron dipoles describing the simulated intersubband transitions are aligned in $\hat{z}$ direction, same as the polarization direction of the incident waves, instead of oriented randomly in three-dimensions space. $g(\nu)$ is the lineshape function which is assumed to be Lorentzian as

$$g(\nu) = \frac{\Delta\nu/2\pi}{(\nu-\nu_0)^2 + (\Delta\nu/2)^2} \tag{2.19}$$

where

$$\Delta\nu = \frac{1}{\pi T_2} = \frac{1}{\pi}\left(\frac{1}{2\tau_i} + \frac{1}{2\tau_f} + \frac{1}{T_2^*}\right) \tag{2.20}$$

is the full-width half maximum (FWHM) linewidth of the transition centered about $\nu_0 = \frac{E_i - E_f}{h}$. T_2 is the total phase breaking time, τ_i and τ_f are the initial and final state lifetimes, and T_2^* is the pure dephasing time.

With the stimulated emission rate, the small signal bulk optical gain per unit length for a transition with a population inversion per unit volume ΔN is written as:

$$\gamma(\nu) = \frac{h\nu}{c/n}\frac{W_{i\to f}^{(st)}}{I(\nu)}\Delta N = \frac{3\lambda^2}{8\pi n \tau_{i\to f}^{(sp)}}\Delta N g(\nu) \tag{2.21}$$

The peak gain is

$$\gamma_{max} = \gamma(\nu_0) = \frac{3\lambda^2}{4\pi^2 n \tau_{i\to f}^{(sp)}}\frac{\Delta N}{\Delta\nu} \tag{2.22}$$

which is consistent with Eq. 1.7 with Eq. 1.5, Eq. 2.14 and Eq. 2.16 substituted into Eq. 2.22.

2.2.3 Inter- and intra-subband nonradiative transitions

The design of QCLs relies on engineering the scattering rates to tailor the electron lifetime at key energy levels to provide a population inversion. The longitudinal optical (LO) phonon scattering, or sometimes donated as transition, is the dominant nonradiative scattering mechanism among all. And the majority of QCLs are designed based on the fast LO phonon emission-assisted depopulation of lower laser levels, which can reduce a low laser level lifetime to be smaller than one picosecond (ps). This section presents the theoretical calculation of LO phonon scattering rate, based on Ref. [18].

The LO phonon scattering can happen both between two subbands and within one subband. This is nonradiative transition and satisfies the conservation of in-plane momentum and energy as:

$$\mathbf{k_i} = \mathbf{k_f} + \mathbf{q}_{\|} \tag{2.23}$$

$$E_i(\mathbf{k_i}) = E_f(\mathbf{k_f}) \pm \hbar\omega_{LO} \tag{2.24}$$

where + stands for emission of a phonon and − stands for absorption of a phonon. $E_{LO} = \hbar\omega_{LO}$ is usually taken to be the Γ-point LO phonon energy in well material (E_{LO}=36.25 meV in GaAs [18], E_{LO}=34 meV in $In_{0.53}Ga_{0.47}As$ [17]). E_i and E_f are the initial and final electron energy. $\mathbf{k_i}$ and $\mathbf{k_f}$ are the initial and final wavevectors in the plane normal to the growth direction for the electron, and $\mathbf{q}_{\|}$ is the in-plane wavevector of the LO phonon emitted. Since the LO phonon branch is taken as dispersionless at the Γ-point, E_{LO} is fixed while $\mathbf{q}_{\|}$ is unlimited. The schematic illustration of intersubband LO-phonon scattering is shown in Fig. 2.2.

Assuming parabolic subband dispersion, the final states lie on a circle with radius k_f determined by

$$k_f^2 = k_i^2 + \frac{2m^*(E_f(0) - E_i(0) \mp \hbar\omega_{LO})}{\hbar^2} \tag{2.25}$$

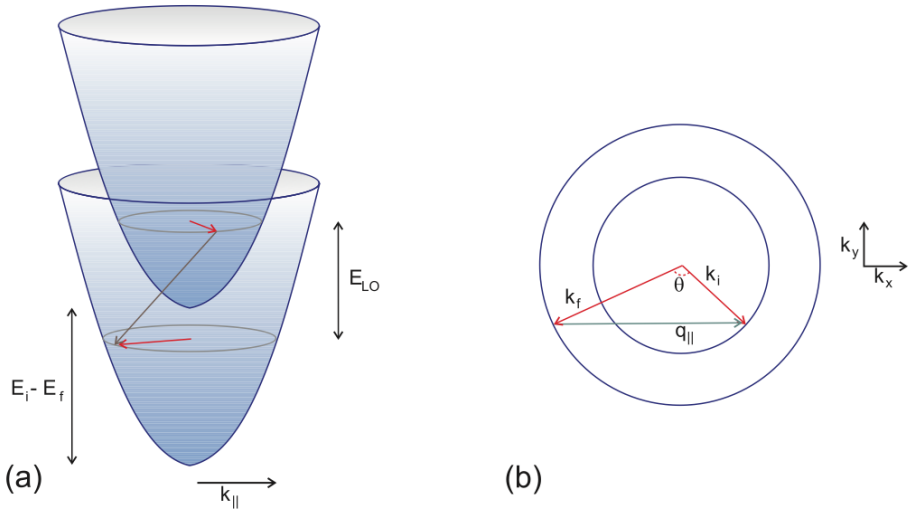

Figure 2.2: (a) Schematic illustration of intersubband LO-phonon scattering process in k-space. (b) In-plane diagram illustrating the relationship between initial and final electron wavevectors k_i and k_f and in-plane phonon wavevector. Figure from [18].

The in-plane momentum conservation requires the in-plane LO phonon wavevector to be

$$q_{\parallel}^2 = |\mathbf{k_i} - \mathbf{k_f}|^2 = k_i^2 + k_f^2 - 2k_i k_f cos\theta \tag{2.26}$$

where the angle θ is the angle between the in-plane wavevector $\mathbf{k_i}$ and $\mathbf{k_f}$ as illustrated in Fig. 2.2.

The electron-LO phonon interaction Hamiltonian takes the form of

$$H' = \alpha(\mathbf{q}) \left(e^{i\mathbf{q}\cdot\mathbf{r}} b_{\mathbf{q}} + e^{-i\mathbf{q}\cdot\mathbf{r}} b_{\mathbf{q}^\dagger} \right) \tag{2.27}$$

where $b_{\mathbf{q}}$ and $b_{\mathbf{q}}^\dagger$ are the creation and annihilation operators for a phonon in mode $\mathbf{q}$. $\alpha(\mathbf{q})$ is the Fröhlich interaction strength for electron-polar-optical-phonon scattering given in SI units as

$$|\alpha(\mathbf{q})|^2 = \frac{\hbar\omega_{LO}}{2} \frac{e^2}{q^2} \left(\frac{1}{\epsilon_\infty} - \frac{1}{\epsilon_{dc}} \right) \tag{2.28}$$

where ϵ_∞ and ϵ_{dc} are the high and static frequency permittivities.

Following Fermi's golden rule and after summation over all the possible phonon modes $\mathbf{q}$, the total LO phonon scattering rate from an initial wavevector is written as:

$$W_{i\to f}^{abs}(\mathbf{k_i}) = \frac{m^* e^2 \omega_{LO}}{8\pi\hbar^2} \left(\frac{1}{\epsilon_\infty} - \frac{1}{\epsilon_{dc}} \right) n_{\omega_{LO}} \int_0^{2\pi} B_{i\to f} d\theta(q_\parallel) \tag{2.29}$$

$$W_{i\to f}^{em}(\mathbf{k_i}) = \frac{m^* e^2 \omega_{LO}}{8\pi\hbar^2} \left(\frac{1}{\epsilon_\infty} - \frac{1}{\epsilon_{dc}} \right) (n_{\omega_{LO}} + 1) \int_0^{2\pi} B_{i\to f} d\theta(q_\parallel) \tag{2.30}$$

where $B_{i\to f}$ is given by

$$B_{i\to f} = \int_\infty^\infty dz \int_\infty^\infty dz' \psi_f^*(z)\psi_i(z)\psi_i^*(z')\psi_f(z') \frac{1}{q_\parallel} e^{-q_\parallel |z-z'|} \tag{2.31}$$

and $n_{\omega_{LO}}$ is the Bose-Einstein distribution as

$$n_{\omega_{LO}} = \frac{1}{exp\left(\frac{\hbar\omega_{LO}}{k_B T}\right) - 1} \tag{2.32}$$

Intrasubband scattering time can be calculated by setting $i = f$. To simplify the calculation, when the transition energy $E_{fi} > E_{LO}$, we can approximate the scattering rate by assuming $k_i = 0$. When $E_{fi} < E_{LO}$, the thermally activated expression can be used to calculate the emission rate

$$W_{i\to f}^{(em)} = W_{i\to f}^{(hot)} e^{\left(\frac{E_{fi}-E_{LO}}{k_B T}\right)} \tag{2.33}$$

where $W_{i\to f}^{(hot)}$ is the scattering rate at the lowest energy E_k in the subband where LO-phonon emission is energetically allowed.

2.3 Bandstructure solver

A bandstructure solver for QCLs based on the shooting (ST) method has been developed by the author using MATLAB language in this thesis, which is presented in this section. This solver provides an effective, efficient and reliable solution to QCLs' bandstructure, radiative transition rates, and LO phonon scattering rates. The nonparabolicity effect is incorporated into the solver without sacrifice of time efficiency, which is the most salient advantage over the numerical finite element matrix solver. LO phonon lifetimes can be further computed based on the eigen-wavefunctions generated by this solver. The accuracy of the ST method-based solver (ST solver) is verified by many examples, two of which are presented in this paper. This solver provides a powerful tool for future QCLs' design.

2.3.1 Shooting method

This section briefly introduces the ST method based on the detailed explanation in [25]. The ST method is a numerical approach to the solution of 1D Schrödinger equation represented as Eq. 2.5. This method is able to find the eigen-energy and eigen-wavefunction at the same time for all the stationary states in a QCL bandstructure, given the well-defined potential profile and effective mass as a

function of z along the growth direction. Eq. 2.5 can be organized into:

$$\frac{\partial}{\partial z}\frac{1}{m^*(z)}\frac{\partial}{\partial z}\psi(z) = \frac{2}{\hbar^2}\left[E_c(z) - E_n\right]\psi(z) \tag{2.34}$$

Let's expand the derivatives in the left side in the above equation in terms of finite difference. We obtain

$$\frac{\frac{1}{m^*(z+\delta z)}\frac{\partial\psi(z)}{\partial z}\big|_{z+\delta z} - \frac{1}{m^*(z-\delta z)}\frac{\partial\psi(z)}{\partial z}\big|_{z-\delta z}}{2\delta z} = \frac{2}{\hbar^2}\left[E_c(z) - E_n\right]\psi(z) \tag{2.35}$$

Recalling the centered finite difference expansion for the first derivative, i.e.

$$\frac{\partial f}{\partial z}\big|_z = \frac{f(z+\delta z) - f(z-\delta z)}{2\delta z} \tag{2.36}$$

Eq. 2.35 can be written as

$$\begin{aligned}\frac{1}{m^*(z+\delta z)}\left[\frac{\psi(z+2\delta z)-\psi(z)}{2\delta z}\right] - \frac{1}{m^*(z-\delta z)}\left[\frac{\psi(z)-\psi(z-2\delta z)}{2\delta z}\right] \\ = \frac{2(2\delta z)}{\hbar^2}\left[E_c(z) - E_n\right]\psi(z)\end{aligned} \tag{2.37}$$

By gathering terms in $\psi(z)$ on the right hand side, then we get

$$\frac{\psi(z+2\delta z)}{m^*(z+\delta z)} + \frac{\psi(z-2\delta z)}{m^*(z-\delta z)} = \left\{\frac{2(2\delta z)^2}{\hbar^2}\left[E_c(z) - E_n\right] + \frac{1}{m^*(z+\delta z)} + \frac{1}{m^*(z-\delta z)}\right\}\psi(z) \tag{2.38}$$

Making the transformation, $2\delta z \to \delta z$ gives

$$\begin{aligned}\frac{\psi(z+\delta z)}{m^*(z+\delta z/2)} = &\left\{\frac{2(\delta z)^2}{\hbar^2}\left[E_c(z) - E_n\right] + \frac{1}{m^*(z+\delta z/2)} + \frac{1}{m^*(z-\delta z/2)}\right\}\psi(z) \\ &- \frac{\psi(z-\delta z)}{m^*(z-\delta z/2)}\end{aligned} \tag{2.39}$$

The continuous wavefunctions are discretized in the z direction by the unit length of δz. With the wavefunction values of the first two points given, all the remaining values in the wavefunction can be computed using Eq. 2.39. Whether such a wavefunction is the eigen solution depends on the choice of E_n and is judged by the boundary conditions. If a wavefunction conforms to the boundary

conditions, this is the eigen-wavefunction and the corresponding energy is the eigen-energy of this wavefunction. The boundary conditions are:

$$\psi(z) \to 0 \text{ and } \frac{\partial \psi(z)}{\partial z} \to 0, \text{ as z } \to \pm\infty \tag{2.40}$$

The initial conditions are given by the first two wavefunction values following the exponentially increasing trend due to its exponential decay into the initial barrier, i.e.

$$\psi(z_0) = 1 \text{ and } \psi(z_0 + \delta z) = exp(\frac{\sqrt{2m^*(E_c(z_0) - E_n)}}{\hbar}\delta z) \tag{2.41}$$

The nonparabolicity effect can be simply incorporated into the solver by making the effective mass profile dependent on the electron energy as shown in Eq. 2.7, which does not increase the algorithm complexity at all.

For a QCL structure to be solved using ST method, the computation time mainly depends on the unit length δz and the range of energy within which the eigen-energy are searched. Same as most numerical solvers based on finite difference method, using a smaller unit size will improve the accuracy of the solution. For most QCL structures, since the thinnest layer is more than 10 Å, the unit length can be safely chosen to be 0.5 Å, which is also used in this thesis work.

2.3.2 Solution to a single square quantum well

The first implementation of the ST method is to solve the localized eigen-state in a single square quantum well. Ref. [26] presents a detailed solution for the single square quantum well structure composed of $Al_{0.37}Ga_{0.53}As/GaAs/Al_{0.37}Ga_{0.53}As$ for various widths. The results of the same problem solved by the ST method is compared with the results shown in [26], with all the material and structures parameters identical with those given in the paper. The nonparabolicity is taken into consideration.

Well Width (Å)	E_n in Ref. [26] (meV)	E_n by ST Solver (meV)	$\Delta\ E_n$ (meV)
5	E_1: 265.27	E_1: 265.27	ΔE_1: 0
20	E_1: 180.90	E_1: 180.89	ΔE_1: -0.01
50	E_1: 81.17 E_2: 254.67	E_1: 81.17 E_2: 254.67	ΔE_1: 0 ΔE_2: 0
100	E_1: 32.30 E_2: 119.52 E_3: 235.79	E_1: 32.30 E_2: 119.52 E_3: 235.79	ΔE_1: 0 ΔE_2: 0 ΔE_3: 0
200	E_1: 10.55 E_2: 41.11 E_3: 88.82 E_4: 149.74 E_5: 218.93	E_1: 10.55 E_2: 41.11 E_3: 88.83 E_4: 149.75 E_5: 218.94	ΔE_1: 0 ΔE_2: 0 ΔE_3: +0.01 ΔE_4: +0.01 ΔE_5: +0.01

Table 2.1: Comparison of eigen-energies solved by the ST solver and the values given in [26] for the same structure.

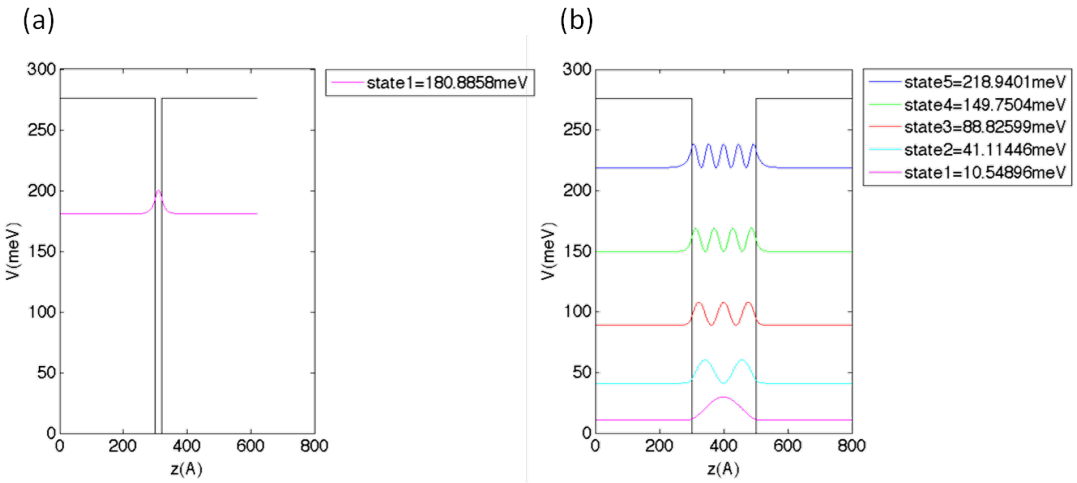

Figure 2.3: The eigen-wavefunctions of localized eigen-states solved by ST solver for (a) a 20 Å-wide well and (b) a 200 Å-wide well.

The bandstructure with eigen-wavefunctions plotted are shown in Fig. 2.3. The initial and last barrier widths are chosen to be 300 Å. This width should be large enough to guarantee the convergence of each eigen-energy, but not too much to avoid the divergence of eigen-wavefunctions at the end of the last barrier due to the precision limit of the computer [25]. The eigen-energies computed by the ST method solver and presented in the Ref. [26] are listed and compared in Table 2.1

This simple example demonstrates the capability of the ST method in solving 1D Schrödinger equation with nonparabolicity incorporated. The time cost for computing the 200 Å-wide well is just 10 seconds by the author's desktop. The precision of the results proves the reliability of this solver.

2.3.3 Solution to QCL bandstructures and transition rates calculation

To further verify the applicability of this ST solver and the relevant transition rates calculation, a mid-IR QCL bandstructure cited from Ref. [4] is used as an

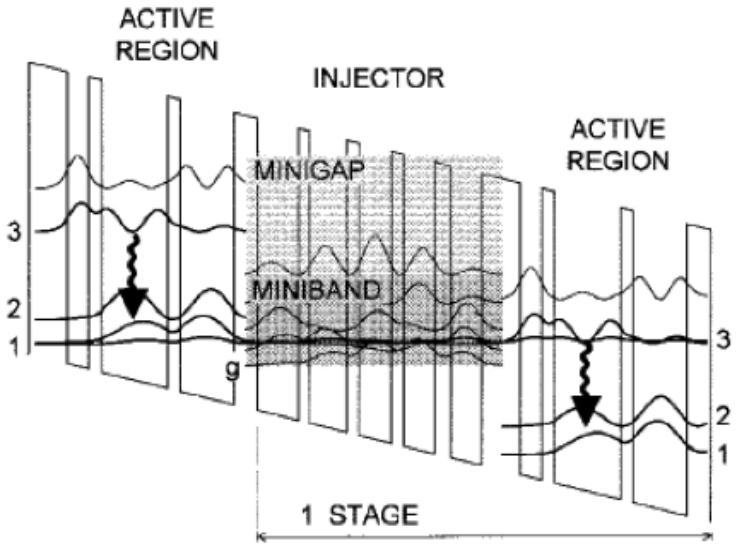

Fig. 1. Conduction band structure of two active regions with the intermediate injector and the moduli squared of the wavefunctions involved in the laser transition (thick lines, labeled "1," "2," and "3") and of the injector wavefunctions manifold (the ground state is labeled g). The laser transition is indicated by the wavy arrows. The layer thicknesses in nanometers of one period of active material and injector are, from left to right starting from the injection barrier (left-most layer in Fig. 1): 3.8/2.1/1.2/6.5/1.2/5.3/2.3/4.0/1.1/3.6/1.2/3.2/1.2/3.0/1.6/3.0. The underlined layers are Si-doped to a level specified in the main text. The applied electric field is 45 kV/cm.

Figure 2.4: The QCL structure presented in Ref. [4].

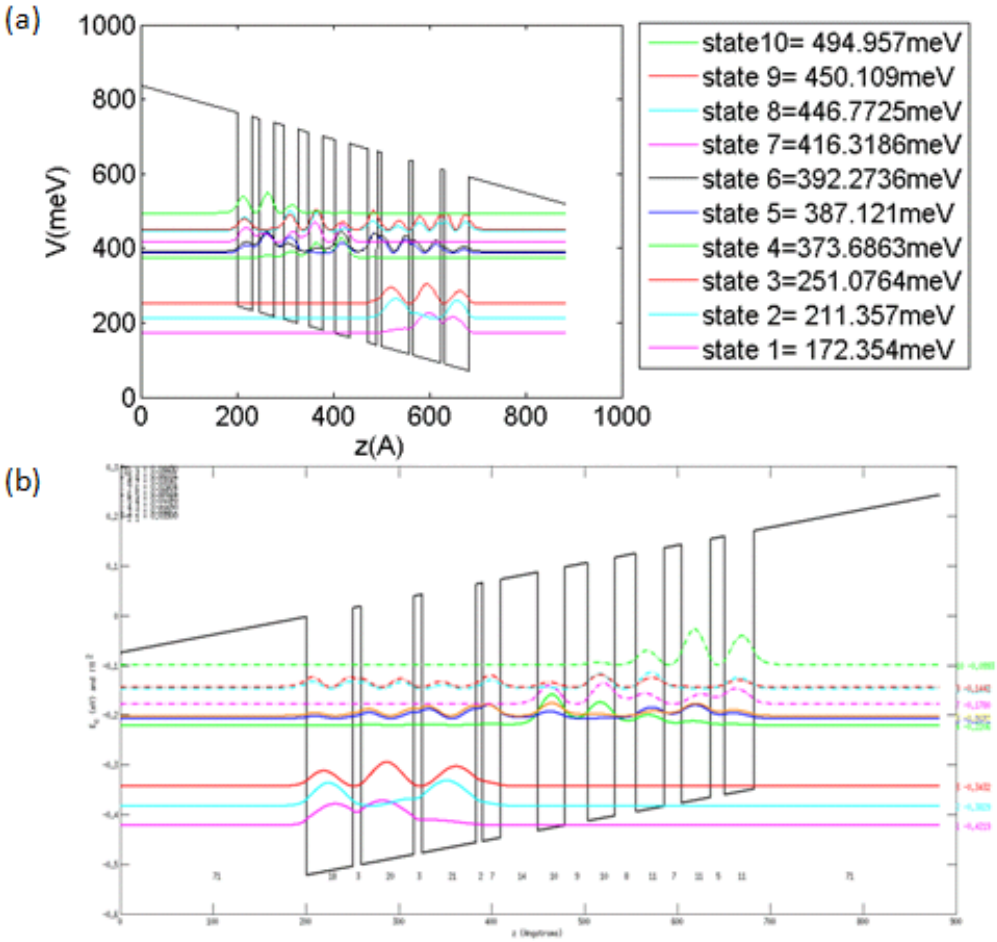

Figure 2.5: Comparison of bandstructures solved by (a) ST solver and (b) Sequal solver for the structure given in Ref. [4].

Energy level index	E_n by Sequal Solver (meV)	E_n by ST Solver (meV)	Δ E_n (meV)
E_1	0	0	0
E_2	39.00	39.00	0
E_3	78.71	78.72	+0.01
E_4	201.34	201.33	-0.01
E_5	214.77	214.77	0
E_6	219.93	219.92	-0.01
E_7	243.97	243.96	-0.01
E_8	274.44	274.42	-0.02
E_9	277.74	277.76	+0.02
E_10	322.64	322.60	-0.04

Table 2.2: Comparison of eigen-energies solved by Sequal solver and ST solver for the structure given in Ref. [4].

τ_{LO}^{em} between two levels at 300K	By Sequal Solver (ps)	By ST Solver (ps)	$\Delta\tau_{ij}$ (ps)
τ_{53}	6.02	6.09	+0.07
τ_{52}	5.58	5.64	+0.06
τ_{51}	8.67	8.55	-0.12
τ_{32}	0.28	0.28	0
τ_{31}	0.86	0.86	0
τ_{21}	0.30	0.30	0

Table 2.3: Comparison of LO lifetimes solved by the ST solver and the Sequal solver for the structure given in Ref. [4].

example for calculation with comparison to the results generated by the Sequal solver used in Ref. [18]. The bandstructure presented in the paper is shown in Figure 2.4, which is based on $In_{0.53}Ga_{0.47}As/In_{0.52}Al_{0.48}As$ system.

The solution of this QCL structure of one module by ST solver and Sequal solver are presented in Figure 2.5 at the same bias (36 kV/cm) as in the paper [4]. The eigen-energy levels solved by these two solvers are compared in Table 2.2, with the lowest eigen-energy level as the base level.

With the eigen-wavefunctions solved, we can move on to calculate various transition rates and lifetimes for the QCL system based on the theoretical work in Section 2.2.2 and 2.2.3. The LO phonon emission lifetimes at 300K between some important energy levels (5, 3, 2 and 1) are calculated based on the two solvers and presented in Table 2.3. The LO lifetime τ_{32} and τ_{21} are $\sim$0.3 ps which is much smaller than other lifetimes. This is due to the effect of resonant LO phonon scattering with the energy spacing between level 3 and level 2, level 2 and level 1 close to the phonon energy ($\sim$34 meV).

CHAPTER 3

QCL ridge waveguide fabrication and modeling

3.1 Introduction

This chapter is focused on the structure and simulation of mid-IR QCL ridge waveguide, and its fabrication processes and results. The two kinds of mid-IR QCLs demonstrated in this work each lases at 9 μm and 4 μm. The standard fabrication procedures have been successfully developed based on the Nanolab facilities in UCLA. The simulation of optical mode in ridge waveguide gives knowledge of waveguide loss and confinement factor.

3.2 Overview of ridge waveguide structures

The ridge waveguide with thin metal top contact is a conventional structure for mid-IR QCLs, the cross section of which is illustrated in Fig. 3.1. The QCL active region sandwiched between upper and lower cladding layers are etched into ridge structure on the top of the InP substrate. Then a thin layer of Si_xN_y or SiO_2 is deposited with a window on top to provide insulation between the voltage applied to the top of the ridge waveguide and its sidewall and substrate. This insulation layer is critical to the lasers' operation; any degradation on this layer will lead to the malfunction of the laser, most likely shorting it. The top and bottom of the waveguide are both deposited with gold (Au) metal with another metal Titanium (Ti) or Germanium (Ge) as thin buffer layer to enable ohmic contact with negligible contact resistance as well as good adhesion [5]. The backside metal

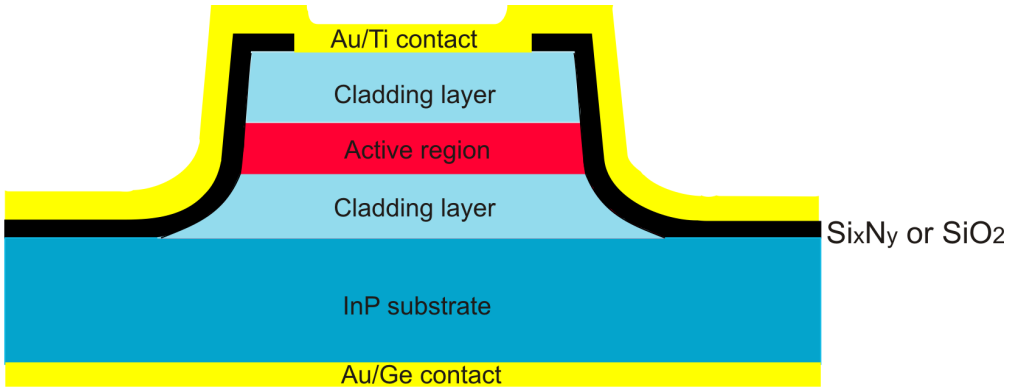

Figure 3.1: Cross section diagram of a ridge waveguide mid-IR QCL

contact is grounded and the top metal contact is wire-bonded to connect to the voltage supply.

3.3 QCL ridge waveguide fabrication

The two kinds of QCL bare wafers (9 μm and 4 μm) are designed and provided by Pranalytica Inc. [29] which is the cooperative partner of this project. The fabrication of QCL ridge waveguide structures is a non-trivial task, including three rounds of photolithography. The overall process for fabrication proceeds are as follows:

1. Define the ridge waveguide structure by photolithography and HBr wet etching. (HBr : HNO_3 : H_2O=1:1:10 in volume)

2. Deposit 300 nm dielectric thin film (Si_xN_y for 9 μm and SiO_2 for 4 μm) on top using PECVD and open a window on the ridge top via second photolithography and AOE dry etching.

3. Define gaps between ridges in metal contact via photolithography and evaporate 20 nm Ti and 300 nm Au on top.

4. Lift off the metal on photoresist, substrate lapping and evaporate 20 nm

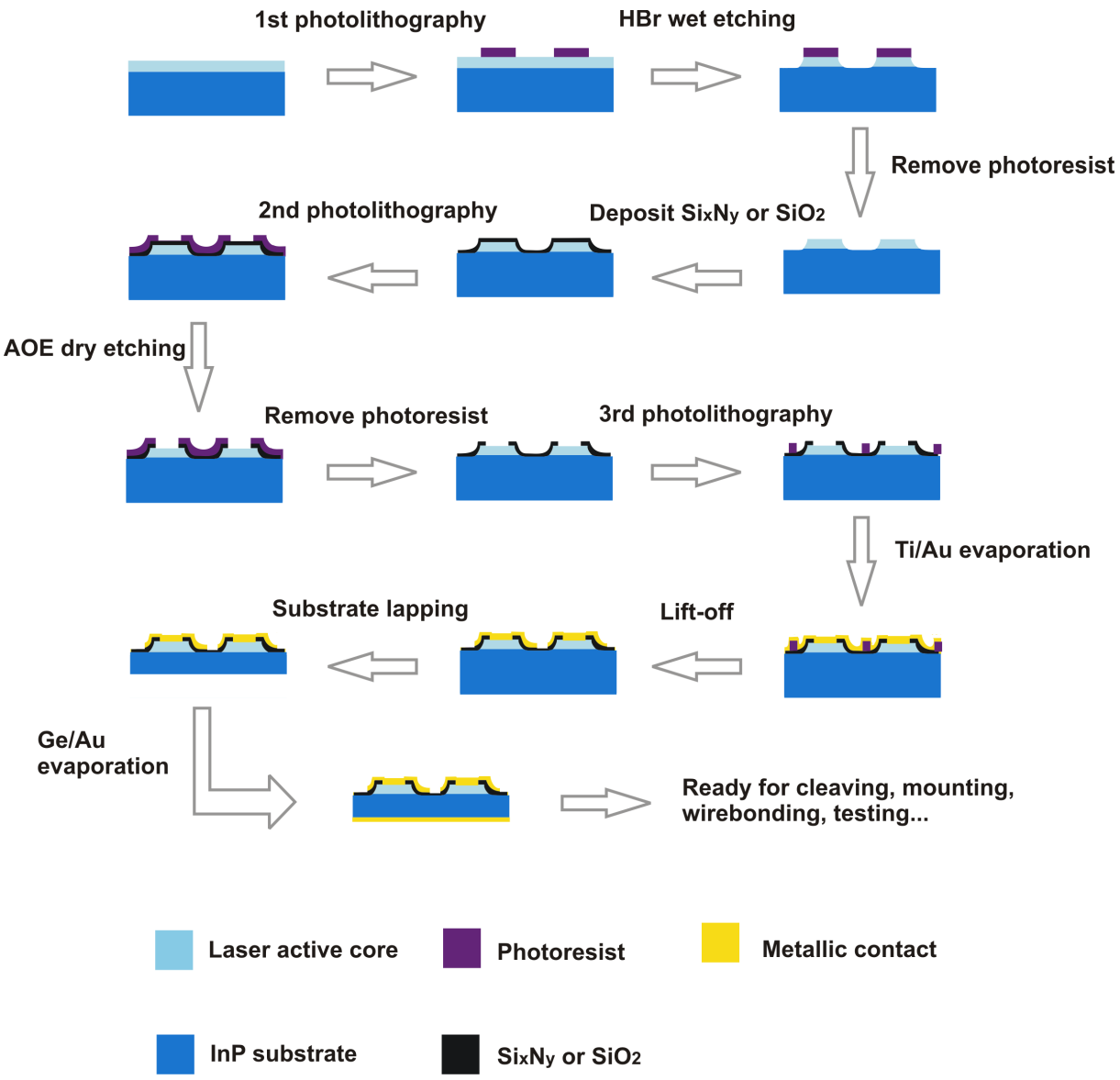

Figure 3.2: Schematic diagram of ridge waveguide QCL fabrication process

	w1 (μm)	w2 (μm)	w3 (μm)	w4 (μm)
Z35 design width	21	24	27	30
Z35 actual width	24.6	25.6	30.5	31.8
Z45 design width	13	15	17	19
Z45 actual width	10.5	12.3	14	16.7

Table 3.1: Comparison of design widths and actual widths for Z35 and Z45 devices.

Ge and 300 nm Au on the backside.

This process flow is illustrated schematically in Fig. 3.2.

3.4 Fabrication results

Ridge waveguide mid-IR QCLs were successfully fabricated, and many devices were successfully tested. Optical microscopic pictures of both two kinds of devices are shown in Fig. 3.3. 9 μm devices are labeled Z35 and 4 μm devices are labeled Z45. The sidewall is not a straight wall, but has a slope towards the substrate due to the wet etching especially for Z35. The wet etching seems to be a little insufficient.

Four different ridge widths are designed on the lithography mask for each wavelength. The actual widths are measured in contrast to the design widths as shown in Table 3.1.

3.5 Optical mode in ridge waveguides

To understand the optical mode distribution in a ridge waveguide, the two-dimensional (2D) electro-magnetic simulation is carried out in COMSOL (version 3.4). The material parameters and thicknesses for each layer in the ridge waveg-

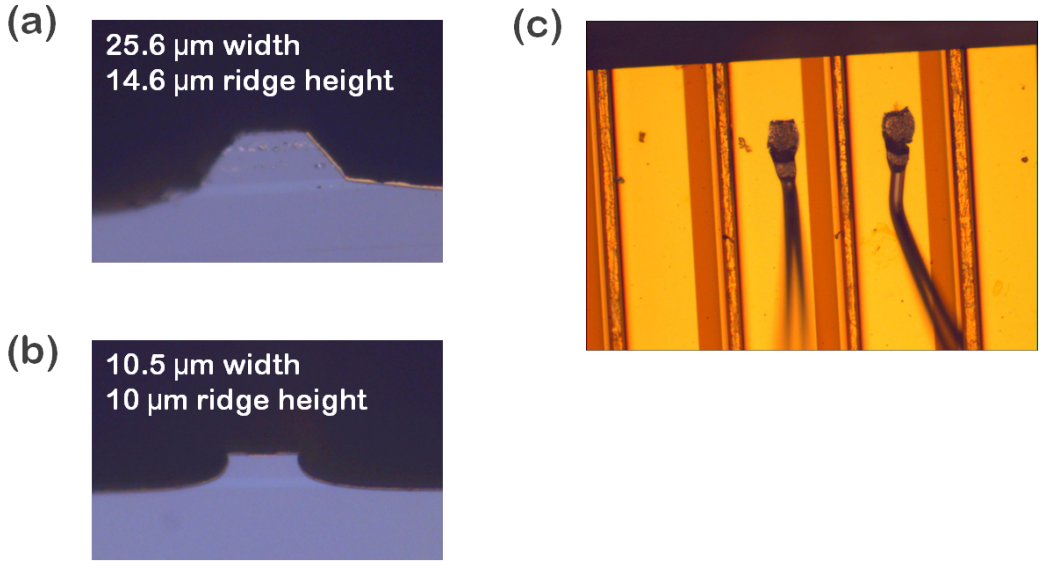

Figure 3.3: Optical microscopic pictures of (a) Z35 and (b) Z45 devices' facets. (c) Top view of the array of Z35 waveguide ridges, two of which are wire-bonded.

uide are provided by Pranalytica Inc by courtesy only for research purpose, which are not presented here due to confidential issue. The permittivity of each layer is calculated based on the Drude model as Eq. 1.11. The electron mobility in each layer's material is calculated based on an empirical low-field mobility model [30] at room temperture (293K). The simulation also gives the knowledge of waveguide loss and confinement factor. However, the active region doping information is lacked. Therefore the simulation results won't reflect the actual waveguide loss in the device tested, but can still reflect the factors that contribute to the loss.

The numerical results of fundamental optical mode distribution are shown in Fig. 3.4 for Z35 and Z45, assuming zero doping in the active region. Table 3.2 shows the simulation results of the waveguide loss and 2D optical confinement factor for Z35 of two kinds of doping and different width corresponding to the fabrication results. The confinement factor is defined as

$$\Gamma = \frac{\int_{active} |E_y|^2 \, ds}{\int_{-\infty}^{\infty} |E|^2 \, ds} \tag{3.1}$$

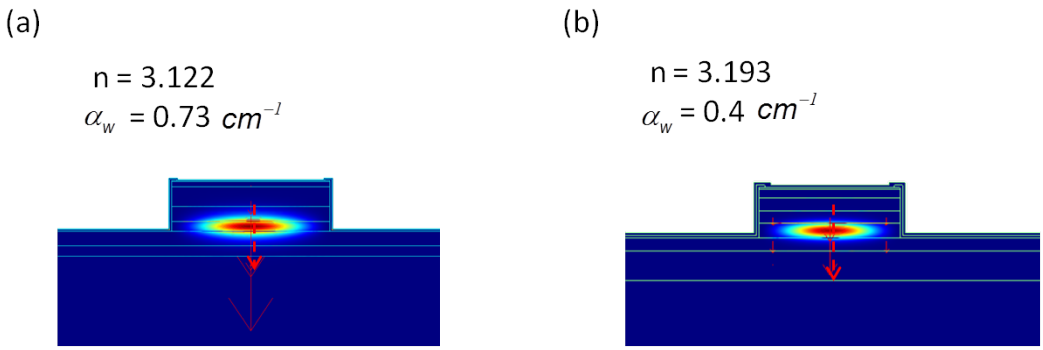

Figure 3.4: Simulation results of fundamental optical mode distribution in Z35 and Z45 ridge waveguides with the red arrow indicating E field direction. The effective refractive index n and waveguide loss α_w are also indicated. (a) $\lambda = 9$ μm, width = 31.8 μm; (b) $\lambda = 4$ μm, width = 16.7 μm. Parameters used in the simulation: refractive index of Au is 10.21+50.2i at $\sim$9 μm and 2.6+24.6i at $\sim$4 μm[31]. Refractive index of noncrystalline Si_3N_4 is 1.8+0.2i at $\sim$9 μm and SiO_2 is 1.38+1.38i at $\sim$4 μm [32].

The waveguide loss in this simulated structure originates in the dielectric layer absorption, the free carrier absorption in gold contact, and the carrier absorption caused by doping in the structure. The active region doping is assumed to be zero and then a moderate doping level (7×10^{14}cm^{-3}) [33]. The comparison between them shows that the doping in the active region just slightly increases the waveguide loss because the doping level is low compared with the doping in the cladding layer. However, when the doping in the cladding layers neighboring to the active region is also assumed to be zero, the waveguide loss for 31.8 μm wide ridge waveguide is reduced to 0.24 cm^{-1}. This suggests that the high-level doping in the cladding layer is an important source of loss. The confinement factor is around 47 % and does not vary much for different ridge width.

Ridge width (μm)	24.6	25.6	30.5	31.8
$\alpha_w(\text{cm}^{-1})$ for doping = 0	0.86	0.83	0.76	0.73
$\alpha_w(\text{cm}^{-1})$ for doping = $7 \times 10^{14}\text{cm}^{-3}$	0.88	0.85	0.78	0.75
confinement factor Γ (%)	47.3	46.8	47.3	47.3

Table 3.2: Simulation results of waveguide loss α_w for zero doping and a usual doping [33] in the active region, and confinement factor Γ (zero doping) for Z35 devices of four different ridge widths at 9 μm wavelength.

CHAPTER 4

Device testing, characterization and discussion

4.1 Introduction

The lasing of Z35 and Z45 are both obtained at room temperature in pulsed mode. Comprehensive testings and characterizations over these devices are conducted in order to extract more information about devices, which are presented in this chapter with a focus on the 9 μm devices Z35. Optical power-Current-Voltage (LIV) measurements are performed at different temperature for devices of different length, which allows for the extraction of waveguide loss and differential modal gain. The lasing spectrum and electroluminescence spectra are measured at different bias. Beam pattern measurement gives a knowledge of the beam quality which is useful for future application of these lasers.

4.2 Device mounting

After fabrication processes, we have pieces of wafer on which arrays of QCL waveguides are lying. Device mounting is also a nontrival work to make a operational QCL device out of such a wafer piece, even though it does not require clean room conditions. Fig. 4.1 shows a Z35 device successfully mounted on a copper submount. The fabricated wafer piece is first cleaved into small dies with two fresh and shining front and rear facets to form a Fabry-Perot cavity. The length of cavity is varied from less than 1 millimeters (mm) to several mm. Each die can contain about 10 to 20 laser ridges. Such a die is mounted on a copper submount

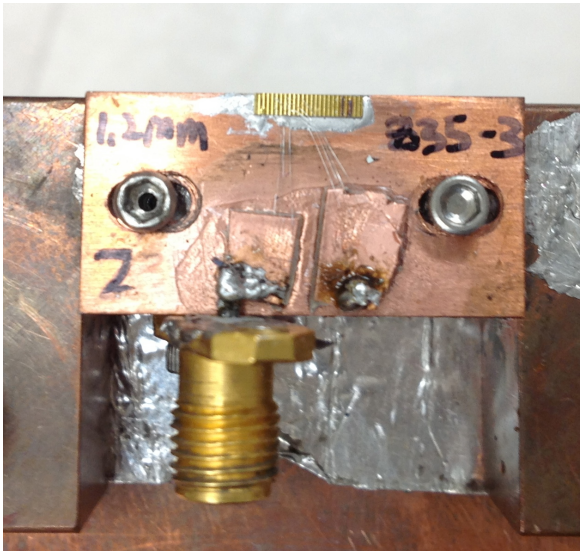

Figure 4.1: Top view of a Z35 device successfully mounted on a copper submount.

via a die bonder with a piece of thin and flattened Indium solder between the die and mount to enhance electrical and thermal conductance. Two copper pads are attached to the copper submount with an insulation dielectric layer in between. Finally the top metal contact of a laser ridge is wire-bonded to the copper pad and a SMA connector is soldered to the pad to set up electrical connection to the power supply.

4.3 LIV measurement and temperature performance

The QCL device on the copper submount is mounted on a thermoelectric (TE) cooler (unit: TE Tech CP-036). The TE cooler can keep stable temperature varied from 20 °C to 80 °C. LIV are collected in this range with a 10 °C increase step. All the date are measured in pulse mode (4 KHz, 200 ns) with a duty cycle of 0.8 % using a high-power pulsed bias supply (unit: AVTECH AVO-6HF). The emitted mid-IR light is coupled via two mid-IR Zinc Selenide (ZnSe) positive meniscus lens (unit: ZC-PM-38-38 ISP optics) to a room-temperature (RT) mer-

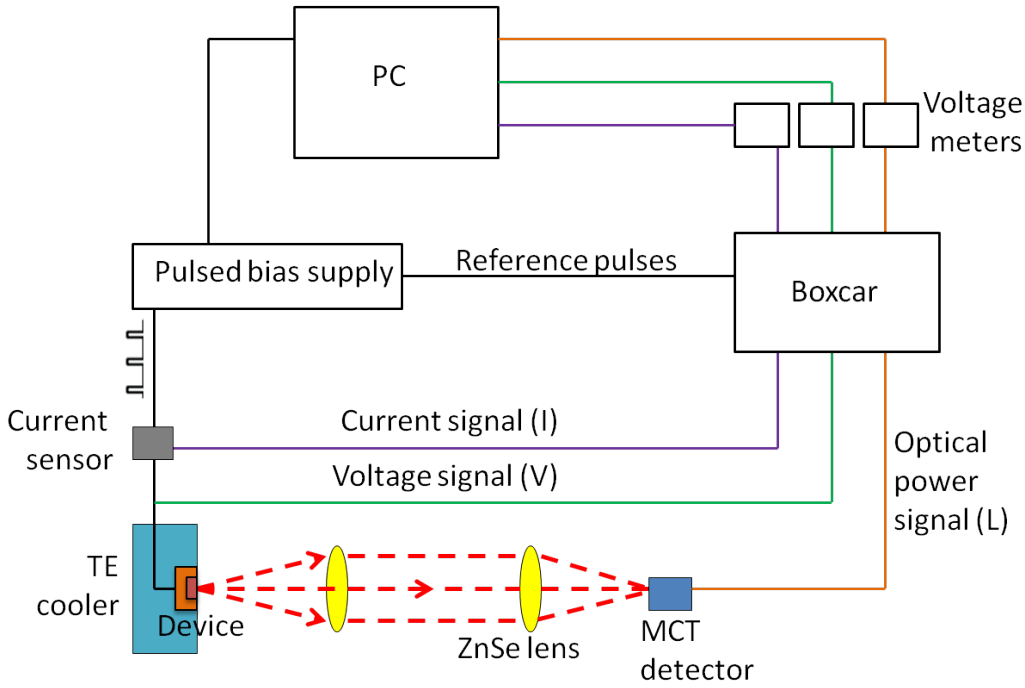

Figure 4.2: Schematic illustration of LIV measurement setup.

cury cadmium telluride (MCT) detector (unit: PEM-10.6 Boston Electronics). The current is probed by an inductive current sensor (unit: 711S IST). The LIV signals are fed into three channels of a boxcar (unit: Ametek Gated Integrator 4121B), which generates three DC voltage output to be read by three voltage meters (unit: Agilent 24410A Digitial Multimeter). The calibration needs to be performed for IV channels in the boxcar in order to relate the DC voltage readings with the actually IV magnitude. The ratio between the actual optical power and the DC voltage output from the boxcar's L channel is determined by measuring the optical power by a thermopile. The measurement setup is illustrated in Fig. 4.2. Peak power is recorded without the correction for the collection efficiency. The collection efficiency is estimated by measuring the total radiation power of the QCL using the thermopile sitting close enough to the QCL's facet, and comparing it with the value measured by the MCT detector after the ZnSe focusing lense. The collection efficiency is approximated around 70 % .

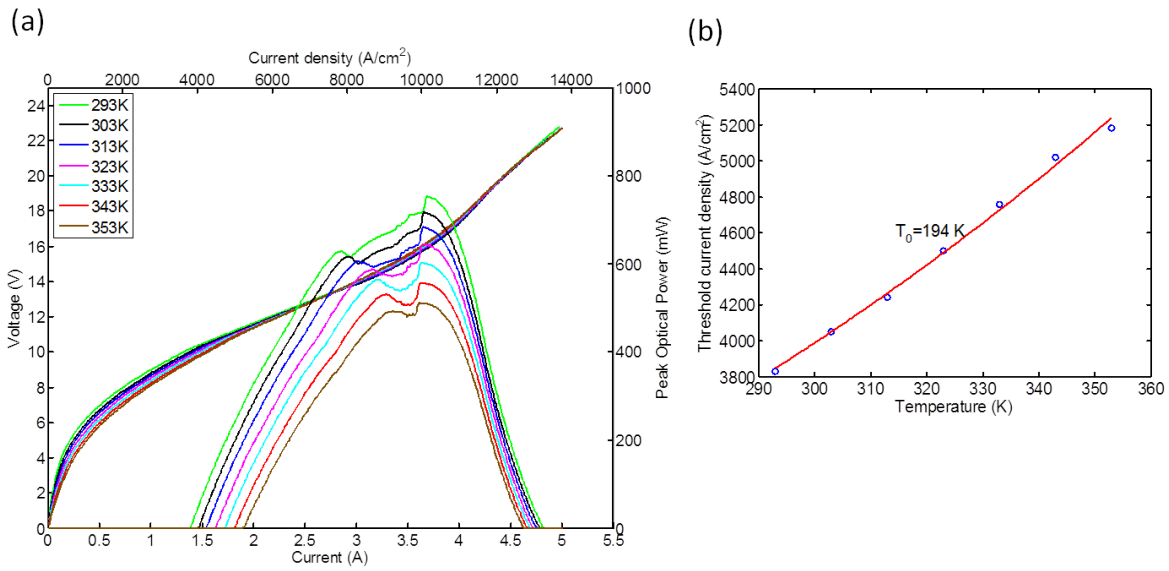

Figure 4.3: (a) LIV measured for a 9 μm device Z353, for which the waveguide length is 1.2 mm, ridge width is 30.3 μm. (b) J_{th} vs. T with T_0 extracted.

The LIV measured for Z35 and Z45 devices, which are respectively labeled as Z353 and Z451 are shown in Fig. 4.3 and Fig. 4.4. The threshold current density J_{th} is extracted from LI curves and plotted with respect to the temperature controlled by the TE cooler. The characteristic temperature T_0 is obtained by fitting J_{th} vs. T with

$$J_{th} = J_{th0} exp(T/T_0) \tag{4.1}$$

T_0 is an indication of temperature performance of a QCL, i.e. how much a QCL will degrade with temperature increased. A high T_0 means less degradation of optical power and slower rise of threshold current with temperature increasing, which is a desired characteristic for a QCL device. T_0 is not just determined by QCLs' active region design, but also its thermal packaging, waveguide design and size. The double-trench ridge waveguide with thick electroplated metal top contact and buried heterostructure laser with selectively area InP regrowth and thick top metal contact are two ideal waveguide structures for much better heat

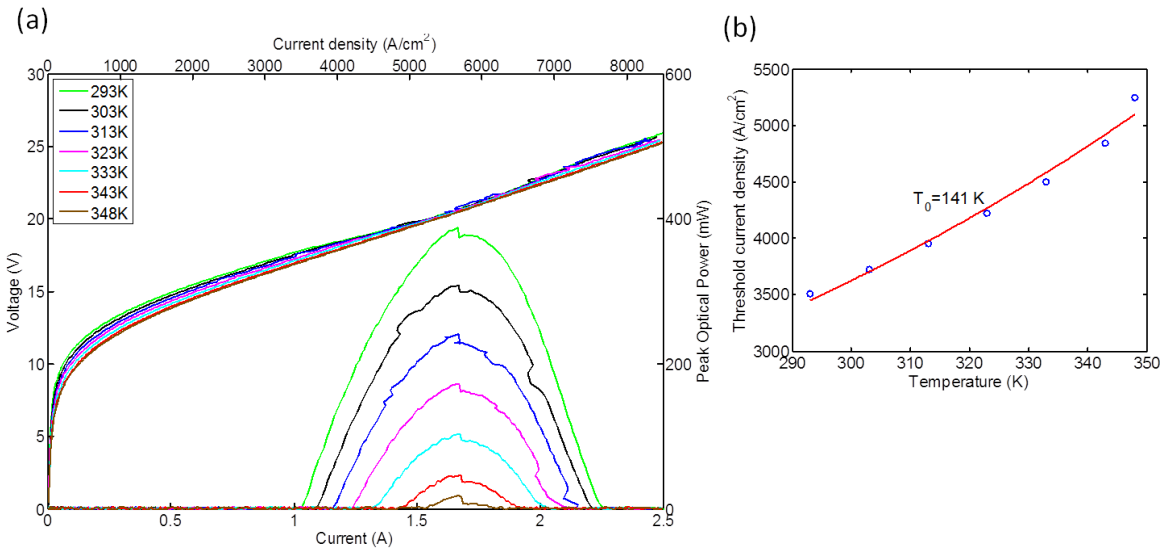

Figure 4.4: (a) LIV measured for a 4 μm device Z451, for which the waveguide length is 2.1 mm, ridge width is 14 μm. (b) J_{th} vs. T with T_0 extracted.

transfer capability and more efficient heat dissipation [17]. These two kinds of waveguides are both mounted epitaxial-side-up to a copper submount with Indium solder. The size of waveguide like its length also has an impact on its temperature performance. Fig. 4.5 shows T_0 extracted for three Z35 devices of same width but different lengths, which are actually cut from the same waveguide. The longer device has a lower T_0, which suggests the less efficient heat dissipation for longer devices.

4.4 Loss and gain measurement

The waveguide loss α_w and differential modal gain Γg_J are obtained based on threshold currenty density and slope efficiency extracted from LIV data for QCLs of same width but different lengths. Reformatting Eq. 1.16 and Eq. 1.18 lead to

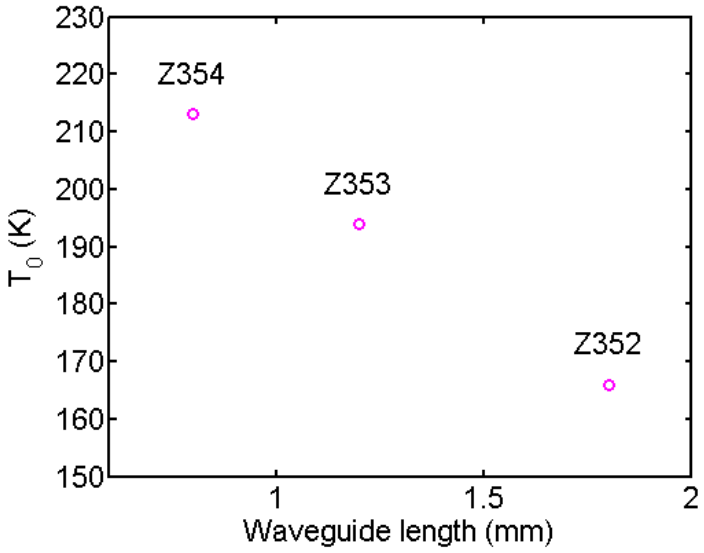

Figure 4.5: Characteristic T_0 extracted for three 9 μm devices of different lengths cleaved from the same waveguide. The ridge width is 30.3 μm. Cavity length for Z352, Z353, Z354 are 1.8 mm, 1.2 mm, 0.8 mm.

the following two equation:

$$J_{th} = J_{tr} + \frac{1}{\Gamma g_J}\left[\alpha_w + \frac{1}{2L} ln(R_1 R_2)\right] = a + b\frac{1}{L} \tag{4.2}$$

$$\left(\frac{dP}{dI}\right)^{-1} = \frac{e}{\hbar\omega N_{mod}} \frac{\tau_2 + \tau_{up}}{\eta\tau_{up} - (1-\eta)\tau_2}\left[1 + \alpha_w \frac{2L}{ln(R_1 R_2)}\right] = c + dL \tag{4.3}$$

By fitting J_{th} as a function of waveguide cavity length to Eq. 4.2 and slope efficiency as a function of cavity length to Eq. 4.3, we can obtain waveguide loss and differential modal gain from the four coefficients a, b, c and d as follows:

$$\alpha_w = \left|\frac{d}{2c} ln(R_1 R_2)\right| \tag{4.4}$$

$$\Gamma g_J = \left|\frac{ln(R_1 R_2)}{2b}\right| \tag{4.5}$$

The waveguide loss and differential modal gain are extracted for 9 μm devices of 30.3 μm wide ridge based on LIV data of three Z35 devices as shown in Fig. 4.5, the results of which are shown in Fig. 4.6. The linear fitting for inverse slope efficiency vs. cavity length is not as good as the fitting for threshold current density, because the measurement of slope efficiency has some deviation caused by the unstable optical coupling efficiency. Thus the waveguide loss α_w extracted is just an approximate number, about 1.5 ± 0.5 cm^{-1}, which is a little higher than the simulation results in Chapter 3. This loss number is comparable to the waveguide loss of similar devices in other studies [33]. However, the determination of threshold current density is much more precise than slope efficiency. Thus the extracted differential modal gain Γg_J is more accurate, which shows its decreasing trend with increased temperature. Γg_J is fitted by $\Gamma g_J = g_0 exp(-T/T_g)$, which gives $T_g = 417$ K. This is an indicator of the decreased upper level lifetime τ_{up} as temperature goes up, since $\Gamma g_J \propto [\eta\tau_{up} - (1-\eta)\tau_2] \approx \eta\tau_{up}$ since $\tau_{up} \gg \tau_2$ (see 1.14). This effect is caused by the increased LO phonon scattering rate for the electrons at the upper lasing level at higher temperature.

Furthermore, the information about transparency current density at threshold can be extracted based on J_{th} vs. cavity length for three Z35 devices for corresponding temperature using Eq. 4.2. The transparency current density for Z35 device of 30.3 μm wide ridge contribute to a considerable part of the threshold current and increases with temperature, as shown in Fig. 4.7. This phenomena is experimentally found in several studies [34, 35], which shows that the transparency current should be considered as an important laser optimization parameter. The fact that the percentage of transparency current in threshold current is larger for longer Z35 device suggests that the electron temperature is actually higher in longer devices, which is consistent with the previous result of less efficient heat dissipation and thus lower characteristic temperature T_0 for longer devices as Fig. 4.5 presents.

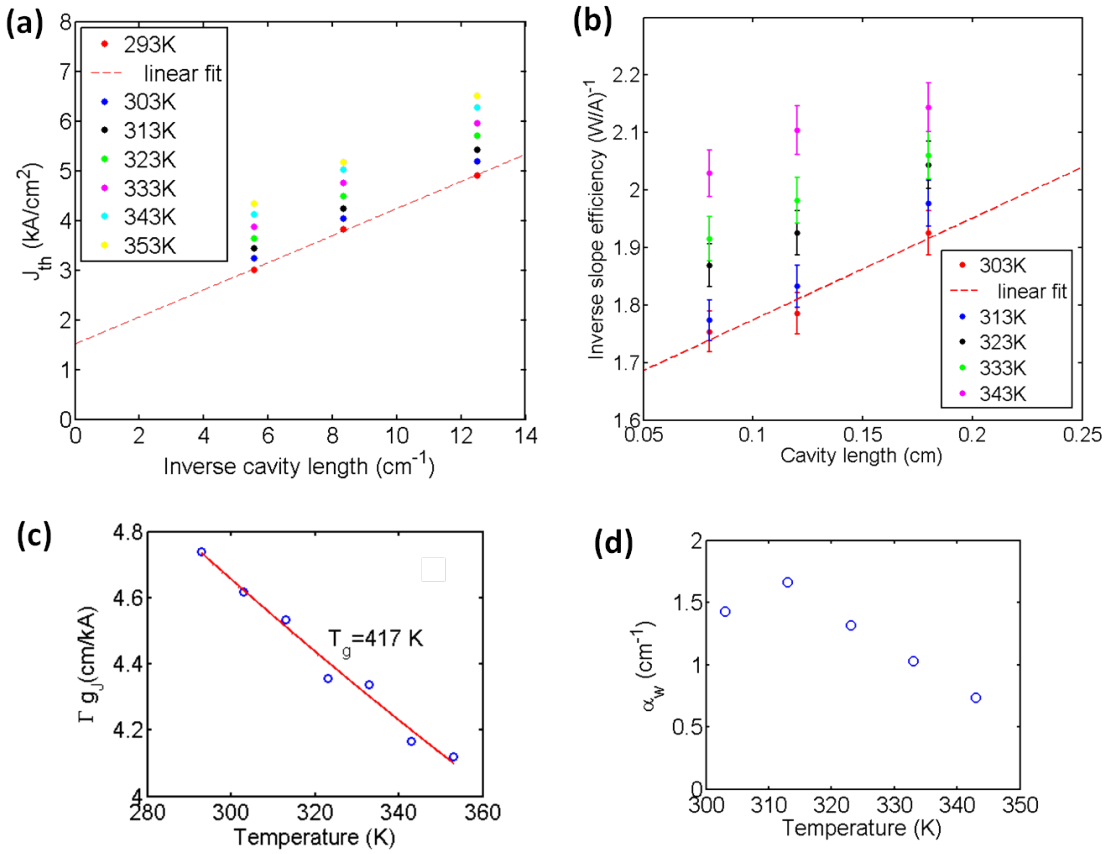

Figure 4.6: (a) J_{th} vs. inverse cavity length and (b) inverse slope efficiency vs. cavity length under different temperature for three 9 μm QCL devices with 30.3 μm wide ridge. (c) Extracted differential modal gain vs. temperature, with its fitting curve (red). (d) Extracted waveguide loss vs. temperature. $R_1 = R_2 = 0.275$ with $n = 0.312$.

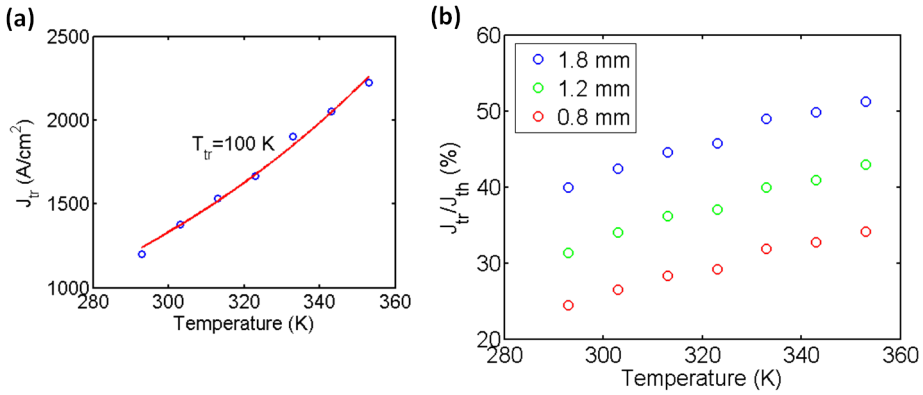

Figure 4.7: (a) Transparency current density J_{tr} vs. temperature extracted for Z35 device of 30.3 μm wide ridge based on LIVs for Z352, Z353 and Z354, as well as the fitting curve (red). (b) The percentage of J_{tr} in J_{th} for Z352, Z353 and Z354 of different cavity length.

Following the rate equation model Eq. 1.1-Eq. 1.3, Eq. 1.16 proposed in Section 1.2.2, the transparency current J_{tr} takes the expression of

$$J_{tr} = \frac{\Delta n_{therm} e}{\eta \tau_{up} - (1-\eta)\tau_2} \propto \frac{\Delta n_{therm} e}{\Gamma g_J} \tag{4.6}$$

which includes the two important factors of transparency current: thermal back-filling of electrons from injector levels to lower lasing level (n_{therm}) and phonon-assisted transition of electron from injector level directly to lower lasing level (η). The third possible cause is escape of electrons to the continuum through injector upper minibands [34], which is not included in this expression but might contribute to J_{tr} measured experimentally. To analyze the effect of the first two causes, J_{tr} is fitted with $J_{tr} = J_{tr0} exp(T/T_{tr})$, which is compared with the fitting for Γg_J vs. T. The result that T_{tr}=100 K is much lower than T_g=417 K suggests that it is the thermal back-filling effect of electrons from injector region to lowering lasing level, rather than the thermal degradation of Γg_J, i.e injection of electrons to the lower lasing level, that primarily causes the rapid increase of transparency current with temperature. This finding implies that the major effort

should be devoted to suppressing thermal backfilling effect in QCL design in order to reduce the considerable transparency current.

4.5 Spectra measurement

The lasing spectra are measured for the 9 μm device at room temperature and different bias using Nicolet Fourier Transform Infrared (FTIR) spectrometer (unit: Nicolet 8700). The spectrum measurement setup is illustrated in Fig. 4.8 (a). Since the lasing intensity is high, the lasing spectrum can be directly resolved by FTIR in the continuous-scan mode and the RT deuterated triglycine sulfate (DTGS) detector (Thermo Nicolet detector) is sufficient in terms of detectivity. The device is lasing in pulsed mode (4 KHz, 200 ns) at RT. The lasing spectra for Z353 at RT under different bias are shown in Fig. 4.9. The laser is lasing in a single longitudinal mode only at very low bias. As bias goes up, it is lasing in multiple longitudinal modes, demonstrating the inhomogeneous broadening nature of mid-IR QCLs which is caused by inhomogeneity in the active region that consists of decades of modules. The spectra get broader and show blue shift as higher bias is applied to the device.

Electroeluminescence (EL) spectra measurement is an approach to measure the bulk gain profile of the active region of QCLs without the cavity filtering effect. Non-lasing mesa samples for Z35 are fabricated, mounted and wire-bonded as shown in Fig. 4.10 (a). A part of the round disk is cleaved away to get rid of the optical cavity feedback. The EL signal from such a sample is very tiny. Therefore, to resolve the EL spectra, the FTIR spectrometer has to be operated in the step-scan mode and a MCT cooled by liquid nitrogen should be used to detect the weak EL signal. A lock-in amplifier (unit: SRS 830 DSP Lock-in Amplifier) is used to read the optical intensity signal at pulsing frequency, as shown in Fig. 4.8 (b). The results of EL spectra at different bias are shown in Fig. 4.10 (b). The

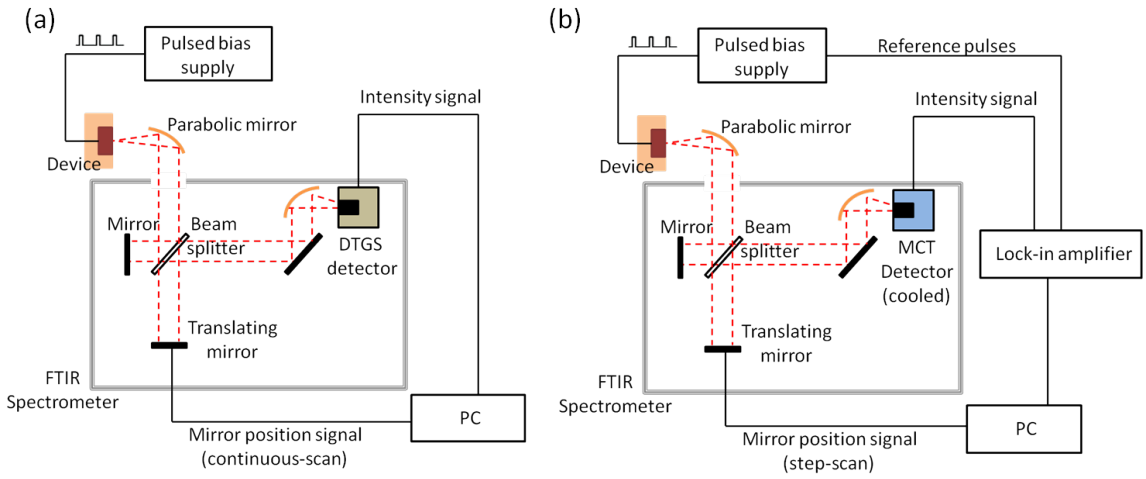

Figure 4.8: Schematic illustration of (a) QCL lasing spectra measurement setup and (b) EL spectra measurement setup.

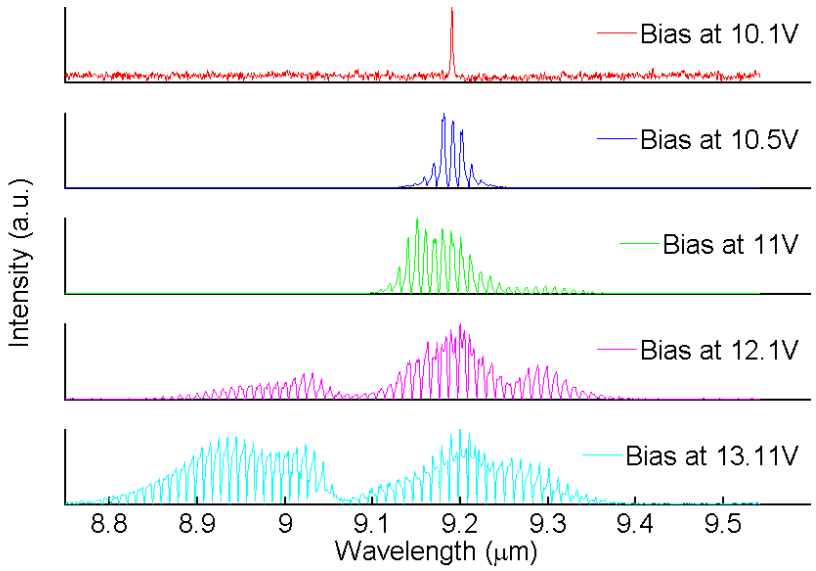

Figure 4.9: Lasing spectra for Z353 at RT under different bias. Z353 is 1.2 mm long and 30.3 μm wide. The spectral resolution is 0.125 cm^{-1}

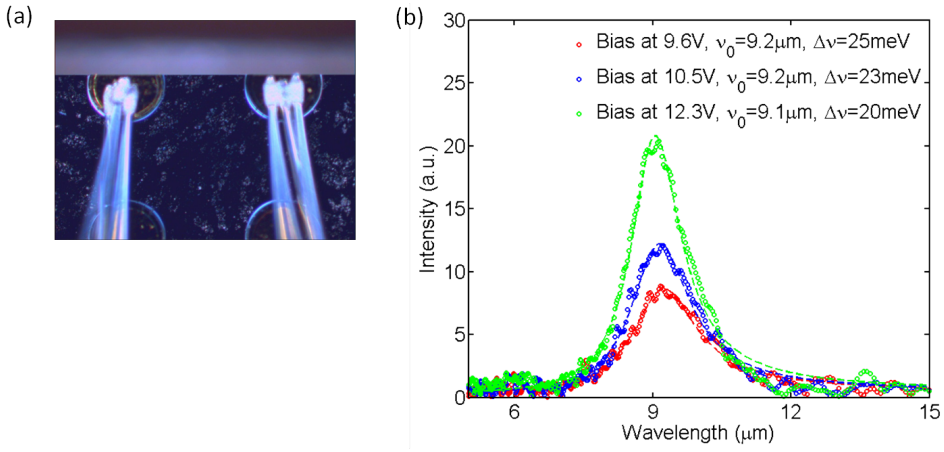

Figure 4.10: (a) The 9 μm disk devices (diameter=208 μm) cut in half for EL measurement at RT. (b) EL spectra and fitting results for the 9 μm mesa piece at RT pulsed at 80 KHz with 200 ns pulse width. The spectral resolution is 16 cm^{-1}.

EL spectra are fitted with Lorentzian function to extract the center frequency and the FWHM, which demonstrates increased peak gain and blue shift of peaks with increased bias.

4.6 Beam pattern measurement

The 2D beam pattern of a 9 μm QCL device is characterized using a 2-axis rotational stage setup. One rotational stage is rotating around z axis to scan angle α, and the other around x axis to scan angle β, with a resolution of 1 °. The QCL device's facet is fixed at the origin of this coordinate as shown in Fig. 4.11 (a), and the RT MCT detector is mounted and driven by the rotation motor to scan in space. The result of 2D beam pattern measurement for device Z354 is shown in Fig. 4.11 (b). The E-plane (along z axis) and H-plane (along y axis) cuts of the 2D beam pattern are shown in Fig. 4.12 and fitted with Gaussian function to extract the beam width. The beam pattern is more divergent in the

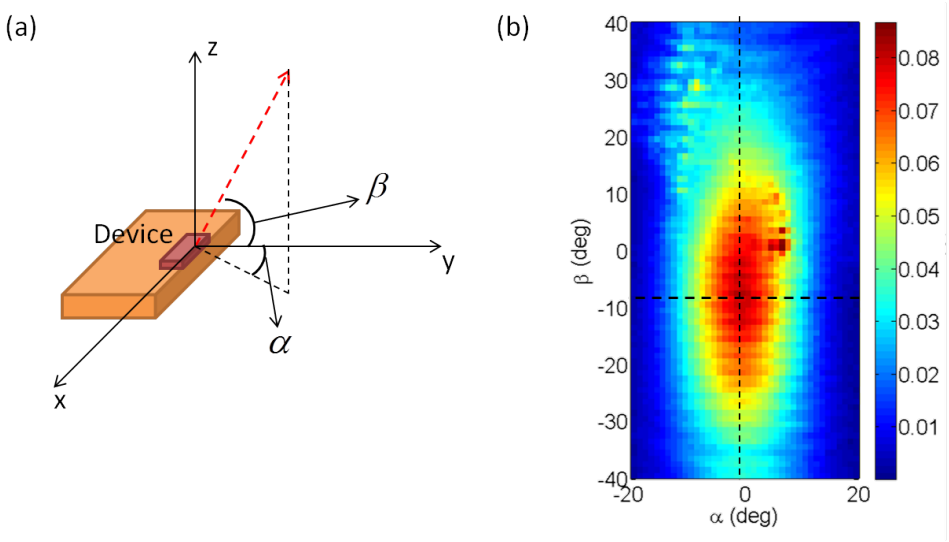

Figure 4.11: (a) Schematic of beam pattern measurement coordinates. (b) The beam pattern measurement result for Z354 at 11.33 V bias and RT.

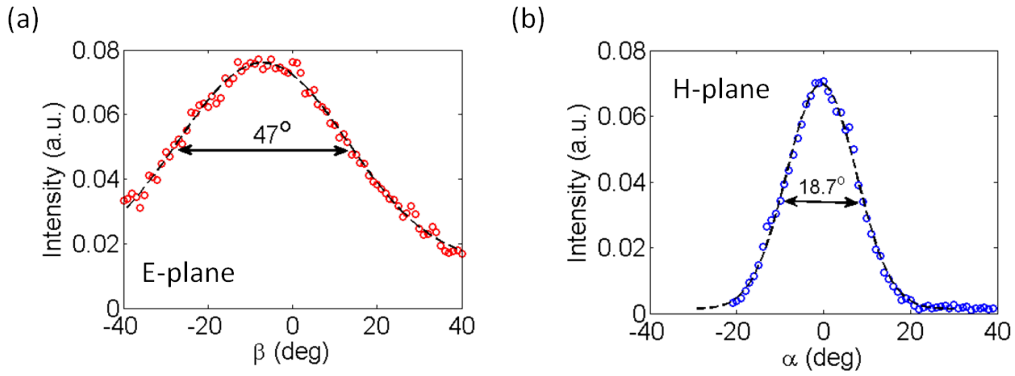

Figure 4.12: E-plane cut (a) and H-plane cut (b) of the 2D beam pattern for Z354 fitted with Gaussian function.

z direction because of the stronger mode confinement by the small active region thickness ($\sim$2 μm) in this direction compared with the ridge width ($\sim$30 μm).

CHAPTER 5

Conclusions

In this work, a comprehensive study over mid-IR QCLs has been conducted which involves background review, theoretical modeling, numerical simulation, microfabrication, and experimental characterization and testing. This study not only leads to an in-depth understanding of QCLs' theory and mastery of practical techniques, but also brings out some interesting findings that contribute to the future design improvement. Some of the major accomplishments and experimental observations that were achieved throughout the course of this research includes:

- An efficient and reliable numerical computational tool has been developed to solve 1D wavefunctions in a QCL bandstructure based on the shooting method. The nonparabolicity effect can be easily incorporated into this method without requiring more computation time. Radiative transition rate and non-radiative phonon scattering rate can be accurately calculated based on the wavefunctions solved by this computational tool.

- Two sets of mid-IR QCL devices lasing at 9 μm and 4 μm have been successfully fabricated using UCLA Nanolab facilities, and both demonstrated lasing at RT in pulsed mode. A reliable fabrication process flow for the ridge waveguide mid-IR QCL has been developed.

- The ridge waveguide structure has been modeled numerically in COMSOL, which generates the numerical results for the optical mode, waveguide loss and confinement factor for different structure dimensions and choices of

doping. The simulation results reveal that the high doping in cladding layers is the major cause of the waveguide loss.

- Several testing setups for mid-IR QCLs have been built up in this work to characterize various properties of devices. Lots of measurement have been done, including LIV measurements at different temperature, loss and gain measurement, lasing and EL spectra measurement, as well as beam pattern measurement.

- Transparency current has been extracted from measurement data, which turns out to be a considerable component in the total current. The analysis of transparency current and differential modal gain reveals and compares the impact upon the devices' temperature performance caused by reduced upper lasing level lifetime and thermally excited electrons backfilled to the lower lasing level. These findings imply that the key to the suppression of transparency current at high temperature is to limit the thermal backfilling effect.

Although mid-IR QCLs have already been available commercially, it is still an interesting area for scientific exploration to achieve further improvement in its high-temperature performance, wall-plug efficiency and tunability. The application range for mid-IR QCLs is also waiting for more extensive exploration. The future work following this research is to make use of these mid-IR QCL devices to set up a mid-IR ellipsometric measurement system for the study over a novel material - topological insulators.

APPENDIX A

Processing recipes

A.1 AZ5214E Photolithography

1. HMDS vaporization for 8 minutes.

2. Deposit AZ5214E. Spin at 600 rpm, 100 rpm/s for 6 seconds; 4000 rpm, 1000 rpm/s for 40 seconds.

3. Wafer bake at 110 °C for 1 minute on hotplate.

4. Kaul-Suss exposure at 8 W/cm^2 for 10 seconds; hard contact gap is 20 μm.

5. Developing in V(AZ400K): V(H_2O)=1:4 for 60 seconds. DI water rinsing. Blow dry with N_2.

A.2 NLOF 2020 Photolithography

1. Deposit NLOF 2020. Spin at 500 rpm, 100 rpm/s for 6 seconds; 2000 rpm, 500 rpm/s for 6 seconds; 4000 rpm, 1000 rpm/s for 30 seconds.

2. Wafer bake at 110 °C for 1 minute on hotplate.

3. Kaul-Suss exposure at 8 W/cm^2 for 12 s; hard contact gap is 35 μm.

4. Developing in 100 % AZ300MIF for 70-80 seconds. DI water rinsing. Blow dry with N_2.

A.3 PECVD growth recipe

Si_3N_4 growth: use LFSINST recipe. Deposition rate is 375 Å/min.

SiO_2 growth: use LFSIOST recipe. Deposition rate is 420 Å/min.

1. A dummy silicon wafer should be used to test the recipe before running it on the real sample. Check the thickness of the film grown on the wafer by Filmtek 2000, with another bare silicon wafer as the reference.

2. Use BOE to etch the oxide on the sample for 1 minute before PECVD growth. DI wafter rinsing. Blow dry with N_2. This should be done no earlier than 20 minutes before growth.

3. Run the recipe on the real sample together with another bare dummy silicon wafer piece which will be used to test the dry etching recipe.

A.4 Dry etching recipe

Si_3N_4: use SIN4000 recipe. Etch rate is 4000 Å/min.

SiO_2: use SIN4000 recipe. Etch rate is 4000 Å/min.

1. Put samples into Tegal Plasma Stripper and run it at 100 W for 1 minute. Pressure is 0.5 Torr.

2. Put enough thermal grease on the silicon wafer and stick the sample onto it. Press the opposite corners of the sample a little bit to make a good thermal contact.

3. Put the dummy silicon wafer with Si_3N_4 or SiO_2 grown on it together with the corresponding sample. The color on the dummy wafer indicates whether the etching is sufficient to remove all the dielectric layer or not.

References

[1] F. Capasso, C. Gmachl, D. L. Sivco, and A. Y. Cho. Quantum cascade lasers. *Physics Today,* 34-40, May 2002.

[2] J. Faist, F. Capasso, D. L. Sivco, C. Sirtori, A. L. Hutchinson, and A. Y. Cho. Quantum cascade lasers. *Science,* Vol. 264, 553-556, 22 April 1994.

[3] B. Williams. Terahertz quantum-cascade lasers. *Nature Photonics,* Vol. 1, 517-525, Sept 2007.

[4] J. Faist, D. Hofstetter, M. Beck, T. Aellen, M. Rochat, and S. Blaser. Bound-to-Continuum and Two-Phonon Resonance Quantum-Cascade Lasers for High Duty Cycle, High-Temperature Operation *IEEE Journal of Quantum Electronics,* Vol. 38, No. 6, 533-546, June 2002.

[5] M. Razeghi. High-Performance InP-Based Mid-IR Quantum Cascade Lasers. *IEEE Journal of Selected Topics in Quantum Electronics,* Vol. 15, No. 3, 941-951, May/June 2009.

[6] P. H. Siegel. Terahertz Pioneer: Federico Capasso "Physics by Design: Engineering Our Way Out of the THz Gap". *IEEE Transactions on Terahertz Science and Technology,* Vol. 3, No. 1, 6-13, Jan 2013.

[7] W. Chen, J. Cousin, E. Poullet, J. Burie, D. Boucher, X. Gao b, M. W. Sigrist, and F. K. Tittel. Continuous-wave mid-infrared laser sources based on difference frequency generation. *C. R. Physique (2007),* doi:10.1016/j.crhy.2007.09.011

[8] R. W. Waynant, I. K. Ilev and I. Gannot. Mid-infrared laser applications in medicine and biology. *Phil. Trans. R. Soc. Lond,* 359, 635-644, A 2001.

[9] http://www.laserfocusworld.com/articles/print/volume-47/issue-8/features/photonics-applied-defense-ir-countermeasures-aim-for-safer-flights.html

[10] M. Tacke. Lead-salt lasers *Phil. Trans. R. Soc. Lond,* 359, 547-566, A 2001.

[11] S. B. Mirov, V. V. Fedorov, I. S. Moskalev, and D. V. Martyshkin. Recent Progress in Transition-Metal-Doped IIVI Mid-IR Lasers. *IEEE Journal of Selected Topics in Quantum Electronics,* Vol. 13, No. 3, 810-822, May/June 2007.

[12] C. K. N. Patel. Continuous-wave laser action on vibrational-rotational transitions of CO_2. *Physical Review,* Vol. 3, No. 1, 6-13, Jan 2013.

[13] R. F. Kazarinov and R. A. Suris. Possibility of amplification of electromagnetic waves in a semiconductor with a superlattice. *Soviet Physics Semiconductor-USSR,* Vol. 136, No. 5A, Nov 1964.

[14] Y. Yao, A. J. Hoffman, and C. F. Gmachl. Mid-infrared quantum cascade lasers. *Nature Photonics,* Vol. 6, 432-439, June 2012.

[15] Y. Bai, N. Bandyopadhyay, S. Tsao, S. Slivken, and M. Razeghi. Room temperature quantum cascade lasers with 27% wall plug efficiency. *Applied Physics Letter,* 98, 181102, 2011.

[16] Y. Bai, S. Slivken, S. Kuboya, S. R. Darvish and M. Razeghi. Quantum cascade lasers that emit more light than heat. *Nature Photonics,* Vol. 3, 99-102, Feb 2010.

[17] Z. Liu. *Room-temperature, continuous-wave quantum cascade lasers in the first and second atmospheric windows.* PhD dissertation, Princeton University, Department of Electrical Engineering, 2008.

[18] B. Williams. *Terahertz quantum cascade lasers.* PhD dissertation, Massachusetts Institute of Technology, Department of Electrical Engineering and Computer Science, 2003.

[19] J. Faist. Wallplug efficiency of quantum cascade lasers: Critical parameters and fundamental limits. *Applied Physics Letter,* 90, 253512, 2007.

[20] R. Maulini, A. Lyakh, A. Tsekoun, and C. K. N. Patel. $\lambda\sim7.1$ μm quantum cascade lasers with 19% wall-plug efficiency at room temperature. *Optics Express,* Vol. 19, No. 18, Aug 2011.

[21] I. Vurgaftmana, J. R. Meyer, and L. R. Ram-Mohan. Band parameters for IIIV compound semiconductors and their alloys. *Journal of Applied Physics,* Vol. 89, No. 11, June 2001.

[22] H. C. Liu, and F. Capasso. *Intersubband Transitions in Quantum Wells: Physics and Device Applications.* Academic Press, Vol. 62, 2000.

[23] H. C. Liu, and F. Capasso. *Intersubband Transitions in Quantum Wells: Physics and Device Applications.* Academic Press, Vol. 66, 2000.

[24] L. A. Coldren, and S. W. Corzine. *Diode lasers and photonic integrated circuits.* John Wiley & Sons, 1995.

[25] P. Harrison. *Quantum wells, wires and dots.* John Wiley & Sons, 2nd edition, 2005.

[26] D. F. Nelson, R. C. Miller, and D. A. Kleinman. Band nonparabolicity effects in semiconductor quantum wells. *Physical Review B,* Vol. 35, No. 14, May 1987.

[27] R. P. Leavitt. Empirical two-band model for quantum wells and superlattices in an electrical field. *Physical Review B,* Vol. 44, No. 20, 1991.

[28] A. Yariv. *Quantum electronics.* John Wiley & Sons, 3rd edition.

[29] http://www.pranalytica.com

[30] M. Sotoodeh, A. H. Khalid, and A. A. Rezazadeh. Empirical low-field mobility model for III-V compounds applicable in device simulation codes. *Journal of Applied Physics,* Vol. 87, No. 6, Mar 2000.

[31] E. D. Palik. *Handbook of optical constants of solids.* Academic Press, Vol. 1, 1998.

[32] J. Kischkat, S. Peters, B. Gruska, M. Semtsiv, M. Chashnikova, M. Klinkmuller, O. Fedosenko, S. Machulik, A. Aleksandrova, G. Monastyrskyi, Y. Flores, and W. T. Masselink. Mid-infrared optical properties of thin films of aluminum oxide, titanium dioxide, silicon dioxide, aluminum nitride, and silicon nitride. *Applied Optics,* Vol. 51, No. 28, Oct 2012.

[33] A. Lyakh, R. Maulini, A. Tsekoun, R. Go, and C. K. N. Patel. Multiwatt long wavelength quantum cascade lasers based on high strain composition with 70% injection efficiency. *Optics Express,* Vol. 20, No. 22, Oct 2012.

[34] D. G. Revin, R. S. Hassan, A. B. Krysa, K. Kennedy, A. N. Atkins, J. W. Cockburn, Y. Wang, and A. Belyanin. Direct Determination of Transparency Current in Mid-Infrared Quantum Cascade Laser. *CLEO Technical Digest,* 2012.

[35] J. S. Yu, S. Slivken, A. J. Evans, and M. Razeghi. High-performance continuous-Wave operation of $\lambda\sim4.6$ μm quantum-cascade lasers above room temperature. *IEEE Journal of quantum electronics,* Vol. 44, No. 8, Aug 2008.